

# Microscopic study of interlayer magnetic coupling across the interface in antiferromagnetic bilayers

Sandip Halder,<sup>1</sup> Sudip Mandal,<sup>1</sup> and Kalpataru Pradhan<sup>1,\*</sup>

<sup>1</sup>*Theory Division, Saha Institute of Nuclear Physics,  
A CI of Homi Bhabha National Institute, Kolkata-700064, India*

The enhancement of Neel temperature ( $T_N$ ) of low- $T_N$  antiferromagnets in antiferromagnetic bilayers AF1/AF2, where the  $T_N$  of AF1 is larger than AF2 (for example enhancement of  $T_N$  of CoO in CoO/NiO or FeO in FeO/CoO), is a subject of considerable interest. One essential question needs to be answered in these bilayers: is the interfacial coupling a short-range one or long-range that mediates the effect of the AF1 layers on the magnetic properties of AF2 layer? To understand the systematics of the magnetic coupling across the interface, we investigate the plane-resolved magnetotransport properties of antiferromagnetic bilayers using an electron-hole symmetric one-band Hubbard model at half-filling, employing a semi-classical Monte Carlo method. In our model Hamiltonian calculations, we set Coulomb repulsion  $U_1 = 8$  to mimic high- $T_N$  AF1 layer, whereas we use  $U_2 = 2 \times U_1$  to mimic the low- $T_N$  AF2 layer. Our calculations show that the  $T_N$  of the low- $T_N$  antiferromagnet enhances substantially when its thickness is small, similar to experiments, giving rise to single magnetic transition temperature of the bilayer system. These findings are well supported by a single peak in temperature-dependent specific heat. However, for larger thicknesses, the  $T_N$  of the low- $T_N$  antiferromagnet approaches towards its bulk value and constituent antiferromagnetic layers align antiferromagnetically at two separate temperatures and two maxima are observed in specific heat data. Our calculations also show that the delocalization of moments is more or less confined near the interface indicating the short-ranged nature of the proximity effect. Our obtained results are consistent with the experimental observations. A detailed discussion of the modifications that will occur if we use  $U_1 = 8$  and  $U_2 = 0.5 \times U_1$  will also be addressed.

## I. INTRODUCTION

Antiferromagnets (AFs) based on transition metal oxides (TMOs) have garnered renewed interest for their potential in future spintronic devices due to their compelling physical properties<sup>1-4</sup>. Their insensitivity to magnetic fields makes AFs promising candidate for designing magnetic data storage<sup>5-9</sup> and magneto-electronic devices<sup>10</sup>, as they do not create stray fields, thereby enhancing the scalability of the technology of magnetic memory devices<sup>11,12</sup>. In fact, zero magnetic moment of AFs makes them suitable for designing high-density memory integration in spintronic devices<sup>2,13,14</sup>. Subsequently, these AF materials are also useful in advanced random-access memories, magnetic recording and sensor devices<sup>15</sup>. Overall, the physics of AF materials is extremely rich, and occasionally distinct and surprising from their ferromagnetic counterparts.

Despite of the rich physics and numerous practical applications, the majority of antiferromagnetic materials now appear to be inappropriate for use because of their low transition temperature. In order to get around the restriction of operating temperatures in devices, raising the antiferromagnet's transition temperature  $T_N$  has thus emerged as a ongoing area of study<sup>16,17</sup>. The  $T_N$  of AF can be enhanced by implementing a number of techniques, such as: doping, strain, and heterostructure engineering. For instance,  $T_N$  of the magnetoelectric antiferromagnet  $Cr_2O_3$  is enhanced by 10% with just 1% substitution of oxygen by boron anion<sup>18,19</sup>. In  $Cr_2O_3$ , the antiferromagnetic order is established by Cr-Cr di-

rect exchange coupling<sup>20</sup>. Boron doping introduces impurity states that mediate additional strong hybridization between the neighboring Cr ions. As a result, the  $T_N$  of the  $Cr_2O_3$  increases, making it suitable for room temperature applications<sup>21</sup>. Furthermore, the  $T_N$  of the AF  $YMnO_3$  can be enhanced by controlling the strain, achieved by growing  $YMnO_3$  on different substrates<sup>22</sup>. Additionally, by designing ultra-thin heterostructures such as  $[(LaMnO_3)_n/(SrMnO_3)_{2n}]_m$  (with  $n = 1$  and 2), the Neel temperature of the resulting C-type antiferromagnet is increased by  $\sim 70K$  as compared to the solid solution  $La_{1/3}Sr_{2/3}MnO_3$ <sup>23</sup>.

Similar to the enhancement of the ferromagnetic Curie temperature  $T_C$  of diluted magnetic semiconductors when they come into contact with FMs<sup>24-26</sup> or AFs<sup>26,27</sup>, the proximity effect can also be used as an efficient way to increase the  $T_N$  of AF materials. It has also been found that the magnetic proximity effect greatly increases the ferromagnetic  $T_C$  of FM in FM/FM bilayers<sup>28-30</sup>. Additionally, embedding a ferromagnetic Co nanocluster inside a high  $T_C$  ferromagnetic NiFe matrix also increases its  $T_C$ <sup>31</sup>. The Co nanoclusters' magnetic moment was stabilized until room temperature due to the strong exchange interaction at their interfaces with NiFe nanoclusters.

The magnetic vicinity of antiferromagnetic or ferromagnetic (FM) materials actually raises the transition temperature of AF materials, as shown by investigations based on AF/AF<sup>32-35</sup> or FM/AF<sup>36,37</sup> bilayers. So, the augmentation of Neel temperature of one of the AF material in AF/AF bilayers, particularly constructed

with correlated mono-oxide materials and magnetically connected via their interfaces, is a subject of considerable interest. In particular, the bilayer comprising  $NiO$  ( $T_N = 523 K$ <sup>38</sup>, High- $T_N$  AF) and  $CoO$  ( $T_N = 293 K$ <sup>39</sup>, low- $T_N$  AF) is the most well-known system that has been investigated<sup>26</sup> extensively in the last few decades. For smaller thickness of the  $CoO$  layer (less than 20 Å), the  $NiO/CoO$  bilayer acts as a single-phase magnetic system with a single  $T_N$ <sup>33,35,40,41</sup>. These experimental results show that the  $T_N$  of the  $CoO$  layer increases considerably for smaller thickness of the  $CoO$  layer and approaches to the bulk  $T_N$  of  $NiO$ . But, the  $T_N$  decreases with increase of  $CoO$  layer thickness, and as a result, both the  $NiO$  and  $CoO$  show AF transitions at different temperatures. Ultimately, the  $T_N$  of  $CoO$  layer approaches to the bulk limit ( $T_N = 293K$ ) for large thickness. So, overall the  $T_N$  of the bilayer system can be tuned between the temperatures of  $T_N$  of bulk  $NiO$  and  $CoO$ . A similar phenomenon of the enhancement of Neel temperature is also evidenced in bilayers composed of rutile-type antiferromagnets, such as in  $FeF_2/CoF_2$  bilayer<sup>42,43</sup>.

Direct measurements of specific heat of  $NiO/CoO$  superlattices<sup>44,45</sup> show a single peak similar to  $Ni_{0.5}Co_{0.5}O$  alloy for smaller thicknesses that corresponds well with the single magnetic transition temperature of the bilayer system. For thicker bilayers, two broad maxima are observed which are due to different Neel temperatures of the individual  $NiO$  and  $CoO$  layers<sup>45</sup>. As the thickness of the bilayer increases, these two broad maxima eventually approach the individual bulk  $T_N$  of  $CoO$  and  $NiO$ . Several reports on  $NiO/CoO$  bilayers<sup>40,45-48</sup> establish an existence of magnetic couplings at the interface of  $NiO/CoO$  superlattices well above the transition temperature  $T_N$  of  $CoO$ .

As previously stated, the enhancement of low- $T_N$  antiferromagnets is not limited to antiferromagnetic bilayers. The Neel temperature of the antiferromagnet ( $Co_3O_4$ ,  $T_N \sim 40 K$ <sup>49</sup>) also gets enhanced due to the proximity effect of the higher  $T_C$  ferromagnet ( $Ni_{80}Fe_{20}$ ,  $T_N \sim 800 K$ <sup>50</sup>) in  $Ni_{80}Fe_{20}/Co_3O_4$  bilayer<sup>36</sup>. The Neel temperature of  $CoO$  and  $NiO$  also enhances in  $Fe_3O_4/CoO$ <sup>51</sup> and  $Fe_3O_4/NiO$ <sup>52</sup> thin film superlattices, where  $Fe_3O_4$  is a ferrimagnet with high ferrimagnetic curie temperature  $T_c \sim 858 K$ . This enhancement of Neel temperature takes place in the bilayer structure, is associated with the magnetic coupling due to the proximity effect in contact with high transition temperature  $Fe_3O_4$ . Magnetization data of the individual planes of  $CoO$  (not in contact with  $Fe_3O_4$ , i.e., planes which resides far away from the interfaces) shows no enhancement of  $T_N$ , signifies the effect of  $Fe_3O_4$  on the Neel temperature enhancement through the proximity effect is confined to very limited region around the interfaces. There are also evidences of increase orbital magnetic moment of  $Ni$  and  $Fe$  in the interfaces of  $Fe_3O_4/NiO$  superlattice<sup>53</sup>. An exchange interaction is also reported at the interfaces<sup>51,54,55</sup> of antiferromagnet ( $CoO$  or  $NiO$ ) and ferrimagnet ( $Fe_3O_4$ ) superlattices, which shifts the

magnetic hysteresis loop along (or, opposite) to the magnetic field axis, resulted in an exchange bias phenomena. The observed exchange bias field ( $H_{EB}$ ) decreases with increase of temperature and vanishes just above the exchange bias blocking temperature. On the other hand, in the core-shell  $MnO$  ( $T_N \sim 120 K$ )/ $\gamma$ - $Mn_2O_3$  ( $T_C \sim 40 K$ ) nanocomposites, the magnetic moment in the ferrimagnetic shell  $\gamma$ - $Mn_2O_3$  is stable far above  $T_C$  (up to the  $T_N$  of  $MnO$ ) due to the magnetic proximity effect<sup>56</sup>, which is interesting for its unconventional nature. Moreover, in core  $MnO$  - shell  $Mn_3O_4$  nanoparticles, exchange bias effect is evidenced above the ferrimagnetic  $T_C$  of  $Mn_3O_4$ <sup>57</sup>.

What are the benefits of improving the  $T_N$  of the low  $T_N$  AF layer in AF/AF bilayers? For instance, consider the wustite antiferromagnet  $FeO$  ( $T_N \sim 198 K$ <sup>58</sup>).  $Fe/FeO$  bilayers exhibit an exchange bias, shifting the hysteresis loop opposite to the field axis due to exchange interactions at the interface below the  $T_N$  of bulk  $FeO$ <sup>16,59</sup>. However, because of its low  $T_N$ , its potential use in devices is constrained despite its fascinating phenomenon. Growing  $FeO$  on  $CoO$  in  $FeO/CoO$  bilayers enhances its  $T_N$  of the order of  $\sim 100 K$  due to proximity interaction with  $CoO$ <sup>16</sup>. So, the close association of  $CoO$  and  $FeO$  can overcome temperature constraints in device applications. In fact,  $CoO$  proximity also improves the exchange interaction between  $Fe$  and  $FeO$  in  $Fe/FeO$  bilayers, resulting in higher exchange bias and coercive field in the  $Fe/FeO/CoO$  heterostructure. Additionally, the thickness of the  $CoO$  layer significantly affects the exchange bias field ( $H_{EB}$ ) and blocking temperature ( $T_B$ )<sup>16,60-62</sup>. Overall, the proximity of  $CoO$  to  $FeO$  helps overcome temperature constraints in device applications.

Due to their technological significance and the prospect of expanding fundamental understanding the physics of (low- $T_N$ -AF)/(high- $T_N$ -AF) bilayers, particularly at the interface, is of tremendous interest. A microscopic knowledge is required for further advancement in this area. Microscopic analysis can help to determine the number of atomic planes involved in coupling across an interface or if both systems are fully engaged. So, in this article, we aim to understand how the low- $T_N$  antiferromagnetic layer's Neel temperature increases in low- $T_N$ -AF/high- $T_N$ -AF bilayer systems, focusing on the effect of local moment localization/delocalization at the interface. We have employed one-band Hubbard model to investigate the bilayers using semi-classical Monte Carlo (s-MC) technique. We find that the  $T_N$  of the low- $T_N$  antiferromagnet is enhanced significantly for smaller thickness of the low- $T_N$  antiferromagnet. Subsequently, the  $T_N$  of the low- $T_N$  antiferromagnet decreases with increasing its thicknesses and ultimately approaches to the corresponding bulk limit for larger thicknesses of the low- $T_N$  antiferromagnet. For smaller thicknesses of the low- $T_N$  antiferromagnet, the moment delocalization affects its nature, and as a result, the high- $T_N$  antiferromagnet strongly influences the low- $T_N$  antiferromagnet in increasing the

Neel temperature.

The article is arranged as follows: In Sec. **II**, we describe our reference model Hamiltonian and numerical approach for analyzing the properties of antiferromagnetic bilayers. We provide a quick overview of the various physical parameters in Sec. **III** that will be utilized to investigate the magnetic and transport properties of various bilayers. The set of parameter values to build the AF1/AF2 bilayers is subsequently identified in Sec. **IV**. We describe the magnetotransport properties of AF1/AF2 bilayers in Secs. **V** and **VI** in order to shed light on the phenomenon of enhancing the Neel temperature of low- $T_N$  antiferromagnets. Our findings are summarized in Sec. **VII**.

## II. REFERENCE MODEL AND METHODOLOGY

In order to investigate the magnetotransport properties of the (low- $T_N$ -AF)/(high- $T_N$ -AF) bilayers, we consider following electron-hole symmetric one-band Hubbard Hamiltonian:

$$H = -t \sum_{\langle i,j \rangle, \sigma} (c_{i,\sigma}^\dagger c_{j,\sigma} + H.c.) + U \sum_i (n_{i,\uparrow} - \frac{1}{2})(n_{i,\downarrow} - \frac{1}{2}) - \mu \sum_i n_i,$$

where  $c_{i,\sigma}^\dagger$  ( $c_{i,\sigma}$ ) denote the electron creation (annihilation) operator at site  $i$  with spin  $\sigma$  ( $\uparrow$  or  $\downarrow$ ).  $t$  is the hopping amplitude between the nearest neighbors sites.  $U$  is the strength of on-site Coulomb repulsion at site  $i$ .  $n_i = c_{i,\sigma}^\dagger c_{i,\sigma}$  represents the occupation number operator at site  $i$ .  $\mu$  is the chemical potential which controls the overall density of the system. At half-filling ( $n = 1$ ),  $\mu = 0$  in our electron-hole symmetric model Hamiltonian.

Next, eliminating the constant term, we express the Hamiltonian in the following way

$$H = -t \sum_{\langle i,j \rangle, \sigma} (c_{i,\sigma}^\dagger c_{j,\sigma} + H.c.) + U \sum_i n_{i,\uparrow} n_{i,\downarrow} - \frac{U}{2} \sum_i n_i, = H_0 + H_{int}$$

where  $H_0$  contains the non-interacting one-body quadratic part and  $H_{int}$  consists of the interacting quartic part of the model Hamiltonian. Then, to solve the Hamiltonian, we decompose the quartic interaction term into two different quadratic terms as follows:

$$U n_{i,\uparrow} n_{i,\downarrow} = U \left[ \frac{1}{4} n_i^2 - (\mathbf{S}_i \cdot \hat{\Omega}_i)^2 \right]$$

where  $\mathbf{S}_i$  is the spin vector at the  $i$ th site, defined as  $\mathbf{S}_i = \frac{\hbar}{2} \sum_{\alpha,\beta} c_{i,\alpha}^\dagger \sigma_{\alpha,\beta} c_{i,\beta}$  with  $\hbar = 1$ , and  $\sigma$  is the Pauli matrices.  $\hat{\Omega}_i$  is the arbitrary unit vector at site  $i$ . Here, the decoupling is rotationally invariant. Then, the partition function of the model Hamiltonian,  $Z = H_0 + H_{int}$ ,

is written as  $Z = Tr e^{-\beta H}$ , where  $\beta = \frac{1}{T}$  is the inverse temperature with Boltzmann constant  $K_B = 1$ . The window  $[0, \beta]$  is divided into  $M$  number of equally spaced slices of girth  $\Delta\tau$  ( $\beta = M\Delta\tau$ ). To evaluate the partition function, we express  $e^{-\beta(H_0 + H_{int})} = (e^{-\Delta\tau H_0} e^{-\Delta\tau H_{int}})^M$  up to first order in  $\Delta\tau$  using Suzuki-Trotter transformation in the limit  $\Delta\tau \rightarrow 0$  (for very large  $M$ ). Next, by implementing Hubbard-Stratonovich (H-S) transformation, the interacting part of the partition function  $e^{-\Delta\tau U \sum_i [\frac{1}{4} n_i^2 - (\mathbf{S}_i \cdot \hat{\Omega}_i)^2]}$  can be shown to be proportional to

$$\sim \int d\phi_i(l) d\Delta_i(l) d^2\Omega_i(l) \times e^{-\Delta\tau \sum_i \{ \frac{\phi_i(l)^2}{U} + i\phi_i(l)n_i + \frac{\Delta_i(l)^2}{U} - i\Delta_i(l)\hat{\Omega}_i(l) \cdot \mathbf{S}_i \}},$$

for a generic time slice ' $l$ '. Here, the H-S auxiliary fields  $\phi_i(l)$  is coupled with charge density  $n_i$ , and  $\Delta_i(l)$  is coupled with the spin vector  $\mathbf{S}_i$ . Introducing a new vector auxiliary field  $\mathbf{m}_i(l) = \Delta_i(l) \hat{\Omega}_i(l)$ , we evaluate the total partition function as

$$Z = const. \times Tr \prod_{l=M}^1 \int d\phi_i(l) d^3\mathbf{m}_i(l) \times e^{-\Delta\tau [H_0 + \sum_i \{ \frac{\phi_i(l)^2}{U} + i\phi_i(l)n_i + \frac{\mathbf{m}_i(l)^2}{U} - 2\mathbf{m}_i \cdot \mathbf{S}_i \}]}$$

where the product follows the time order product.  $l$  runs from  $M$  to 1. From the partition function, we extract an effective model Hamiltonian. At this moment, we eliminate the  $\tau$  dependence of the classical auxiliary fields and retaining the spatial fluctuations of the auxiliary fields. Then, we use the saddle point value of the auxiliary field  $i\phi_i(l) = \frac{U}{2} \langle n_i \rangle$ . After redefining  $\mathbf{m}_i \rightarrow \frac{U}{2} \mathbf{m}_i$ , we write down the effective Hamiltonian<sup>63-65</sup> as follows

$$H_{eff} = -t \sum_{\langle i,j \rangle, \sigma} (c_{i,\sigma}^\dagger c_{j,\sigma} + H.c.) + \frac{U}{2} \sum_i (\langle n_i \rangle n_i - \mathbf{m}_i \cdot \sigma_i) + \frac{U}{4} \sum_i (\mathbf{m}_i^2 - \langle n_i \rangle^2) - \frac{U}{2} \sum_i n_i - \mu \sum_i n_i. \quad (1)$$

We deal with this spin-fermionic effective model Hamiltonian by diagonalizing the fermionic sector in the fixed background of classical auxiliary fields  $\{\mathbf{m}_i\}$  and  $\{\langle n_i \rangle\}$ . During the Monte Carlo (MC) update, we visit every lattice site sequentially and sampling the classical auxiliary fields  $\{\mathbf{m}_i\}$  using standard Metropolis algorithm. We evaluate  $\{n_i\}$  self-consistently at every 10th step of the MC system sweep. We use 2000 MC system sweeps at a fixed temperature, where the first 1000 MC sweeps are used to thermalize the system and the remaining 1000 MC sweeps are devoted to measuring the physical observables. We discard 10 MC sweeps between the measurements to avoid illicit self-correlation in the data. We

access large system sizes by implementing travelling cluster approximation based Monte Carlo technique<sup>66–70</sup>.

### III. PHYSICAL OBSERVABLES

In order to study the magnetotransport properties of the high- $T_N$ -AF1/low- $T_N$ -AF2 bilayers, we measure various physical observables. Specifically, we calculate the following structure factor associated with quantum spin correlations to estimate the Neel temperatures:

$$S(\mathbf{q}) = \frac{1}{N^2} \sum_{i,j} \langle \mathbf{S}_i \cdot \mathbf{S}_j \rangle e^{-i\mathbf{q} \cdot (\mathbf{r}_i - \mathbf{r}_j)},$$

where  $\mathbf{q}$  is the wave vector and  $N$  is the total number of lattice sites in the system.  $\mathbf{S}_i$  is the quantum spin at site  $i$ , calculated using the eigen values and eigen vectors of the effective Hamiltonian.  $i$  and  $j$  run all over the lattice sites. The angular brackets denote the thermal and quantum mechanical averages of the observables over the Monte Carlo generated equilibrium configurations, along with the configurational averages over the ten initial configurations of the classical auxiliary fields.

The specific heat of the bilayers is calculated by differentiating the total energy of the system with respect to temperature,  $C_v(U, T) = \frac{dE(U, T)}{dT}$ . The central difference formula is applied to estimate the specific heat numerically. We also evaluate the average local moment of the system (a measure of the system averaged magnetization squared) by using the formula:  $M = \langle (n_\uparrow - n_\downarrow)^2 \rangle = \langle n \rangle - 2\langle n_\uparrow n_\downarrow \rangle$ , where  $\langle n \rangle = \langle n_\uparrow + n_\downarrow \rangle$ .

We estimate the density of states (DOS) at a particular frequency  $\omega$ , which is defined as  $DOS(\omega) = \frac{1}{N} \sum_{\alpha} \delta(\omega - \epsilon_{\alpha})$ , where  $\epsilon_{\alpha}$  is the single particle eigen values, and  $\alpha$  runs over the total number ( $= 2N$ ) of eigen values of the system. We implement a Lorentzian representation of the delta function with broadening  $\sim BW/2N$  (where  $BW$  is the bare bandwidth) to enumerate the DOS.

In addition, we calculate the out-of-plane (along z-axis) and in-plane (along x-axis) conductivities of the AF1/AF2 bilayers in the dc limit using the Kubo-Greenwood formalism<sup>71–73</sup>, which is represented by

$$\sigma(\omega) = \frac{A}{N} \sum_{\alpha, \beta} (n_{\alpha} - n_{\beta}) \frac{|f_{\alpha\beta}|^2}{\epsilon_{\beta} - \epsilon_{\alpha}} \delta[\omega - (\epsilon_{\beta} - \epsilon_{\alpha})]$$

where  $A = \pi e^2 / \hbar a$  ( $a$  is the lattice parameter).  $f_{\alpha\beta}$  represents the matrix elements of the paramagnetic current operator  $\hat{j}_z = it \sum_{i,\sigma} (c_{i,\sigma}^{\dagger} c_{i+z,\sigma} - c_{i+z,\sigma}^{\dagger} c_{i,\sigma})$  or,  $\hat{j}_x = it \sum_{i,\sigma} (c_{i,\sigma}^{\dagger} c_{i+x,\sigma} - c_{i+x,\sigma}^{\dagger} c_{i,\sigma})$  between the eigen states  $|\psi_{\alpha}\rangle$  and  $|\psi_{\beta}\rangle$  with corresponding eigen energies  $\epsilon_{\alpha}$  and  $\epsilon_{\beta}$ , respectively, and  $n_{\alpha} = \theta(\mu - \epsilon_{\alpha})$  is the Fermi function associated with the single particle energy level  $\epsilon_{\alpha}$ . Next, the averaged dc conductivity, averaged over a small low-frequency interval ( $\Delta\omega$ ), is determined

as follows:

$$\sigma_{av}(\Delta\omega) = \frac{1}{\Delta\omega} \int_0^{\Delta\omega} \sigma(\omega) d\omega$$

where  $\Delta\omega$  is chosen three to five times larger than the mean finite size gap (average eigen value separation) of the system, which is actually the ratio of the bare bandwidth to the total number of eigen values. All the physical parameters, such as  $U$ ,  $T$ , and  $\omega$ , are measured in units of  $t$ .

To understand the delocalization of local moments across the interface of AF1/AF2 bilayers, we also evaluate the effective hopping parameter (a measure of the gain in kinetic energy)<sup>74,75</sup> along the out-of-plane direction (z-axis) as follows:

$$t_{eff} \equiv \left( \frac{t^{bilayer}}{t} \right)_z = \frac{\left\langle \sum_{i,\sigma} (c_{i+z,\sigma}^{\dagger} c_{i,\sigma} + c_{i,\sigma}^{\dagger} c_{i+z,\sigma}) \right\rangle_{bilayer}}{\left\langle \sum_{i,\sigma} (c_{i+z,\sigma}^{\dagger} c_{i,\sigma} + c_{i,\sigma}^{\dagger} c_{i+z,\sigma}) \right\rangle_0},$$

where angular brackets represent the expectation value in the bilayer system.

### IV. PARAMETER VALUES TO SETUP ANTIFERROMAGNETIC BILAYERS

A bilayer structure made up of two distinct antiferromagnetic layers is depicted in Fig. 1. We characterize the AF1 (AF2) layer by assigning the on-site Hubbard repulsive strength  $U_1$  ( $U_2$ ) and thickness  $w_1$  ( $w_2$ ). We set same hopping parameter ( $t$ ) for both layers. We choose  $U_1$  and  $U_2$  to ensure distinct Neel temperatures for the two layers. Essentially, in our model Hamiltonian calculations, the AF1 (AF2) layer with thickness  $w_1$  ( $w_2$ ) is composed of  $w_1$  ( $w_2$ ) 2D planes with high- $T_N$  (low- $T_N$ ) value. We refer to this AF1/AF2 bilayer structure as the  $w_1/w_2$  antiferromagnetic bilayer (or simply  $w_1/w_2$  bilayer). In the 5/3 (AF1/AF2) bilayer (see Fig. 1), the AF1 (AF2) layer has a thickness of  $w_1 = 5$  and  $w_2 = 3$ . So, in the illustration of 5/3 bilayer, the AF1 layer consists of two edge planes, two middle planes, and one center plane. At the same time the AF2 layer contains two edge planes and one center plane. The hopping parameter ( $t$ ) connects the two layers at the interface. Periodic boundary conditions are considered in all three directions. For 5/3 bilayer we use  $8 \times 8 \times 8$  system for our calculations. In general we set  $8 \times 8 \times w_T$  system, where  $w_T = w_1 + w_2$  for our studies.

First, we examine the well-studied U-T phase diagram for the bulk system to qualitatively capture the key physics of individual AF layers in bilayer systems as illustrated in the inset of Fig. 2(a). We will briefly discuss the necessary basic characteristics of the phase diagram in order to select  $U_1$  and  $U_2$  values to simulate two antiferromagnets while keeping their Neel temperatures in mind. At low temperatures, the bulk system's



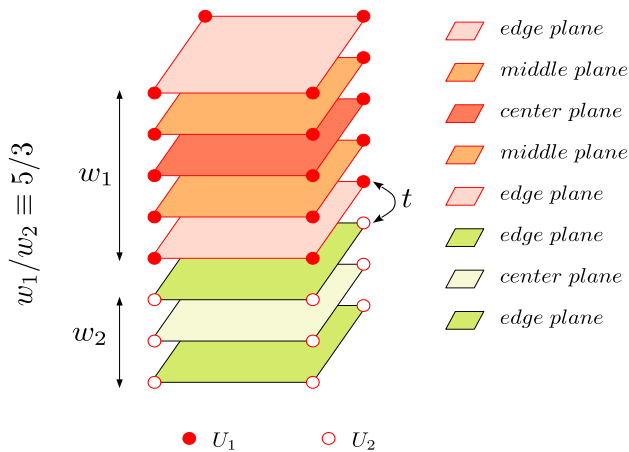


FIG. 1: Schematic representation of AF1/AF2 bilayer system. The red filled (opened) symbol indicates the antiferromagnetic AF1 (AF2) layer. On-site Coulomb repulsion  $U_1$  ( $U_2$ ) is assigned to mimic high- $T_N$ -AF1 (low- $T_N$ -AF2) layer. The antiferromagnetic AF1 (AF2) layer has a thickness of  $w_1$  ( $w_2$ ), indicating the number of planes involved. The bilayer system is referred to as  $w_1/w_2$  bilayer. Different colors are used to denote the edge, middle, and center planes of the AF1 layer. The AF2 layer's edge and center planes are also depicted with two different colors. The hopping parameter  $t$  connects the AF1 and AF2 layers at the interface. This schematic specifically depicts a 5/3 bilayer.

ground state remains in a G-type antiferromagnetic insulating state with finite values of  $U$ . The Neel temperature ( $T_N$ ) exhibits non-monotonic behavior as  $U$  increases. So, the  $T_N$  essentially rises with  $U$  until  $U = 8$  and at that point it reaches its optimal value ( $\sim 0.21$ ). Bulk calculations are performed using  $8 \times 8 \times 8$  system. After  $U = 8$ , the  $T_N$  starts to decrease as  $U$  increases further. The bulk system directly transits from a paramagnetic metallic state to an antiferromagnetic insulating state for  $U < 8$ , meaning that the metal-insulator transition temperature ( $T_{MIT}$ ) and the Neel temperature coincide (i.e.,  $T_{MIT} = T_N$ ). However, for  $U \geq 8$ , the change from a paramagnetic metallic state to an antiferromagnetic insulating state occurs via a paramagnetic insulating state, i.e.,  $T_{MIT} > T_N$ , as the temperature decreases<sup>63,64</sup>. Our findings are in good agreement with earlier findings<sup>63–65,76,77</sup>.

In order to replicate high- $T_N$  AF1 materials, we set the on-site Coulomb repulsive strength  $U_1 = 8$  in our investigation. As mentioned above, for this value of  $U_1$ , the bulk system's ground state stays in an antiferromagnetic insulating state with a high  $T_N$  ( $\sim 0.21$ ). Additionally, we fix the AF1 layer's thickness at  $w_1 = 5$ . By altering the on-site Hubbard repulsive strength  $U_2$  and thickness  $w_2$  of the AF2 layer, we examine the magnetotransport properties of bilayer systems.

We will now briefly present the modification of the bilayer's  $T_N$  by altering  $U_2$  values. Fig. 2(a) shows the  $T_N$  of the AF2 layer of the 5/1 bilayer, as well as the  $T_N$  of

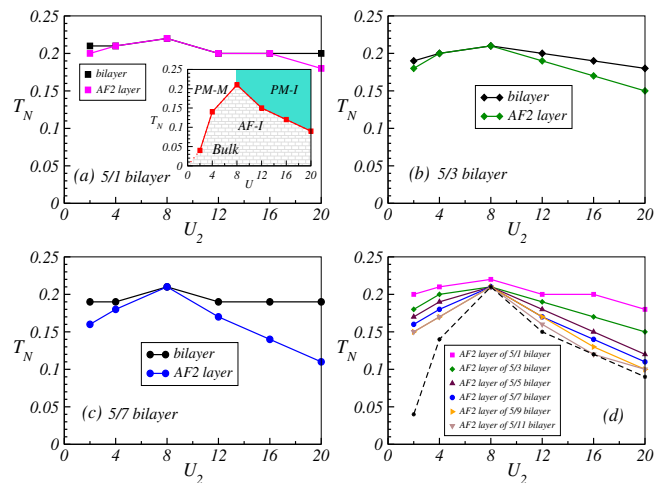


FIG. 2: The variation of Neel temperature  $T_N$  [obtained from  $S(\pi, \pi, \pi)$  vs  $T$  calculations] of the whole bilayer and the constituent AF2 layer with increasing the  $U_2$  value in the AF2 layer is plotted for (a) 5/1 bilayer, (b) 5/3 bilayer, and (c) 5/7 bilayer. We set  $U_2 = 8$  to mimic the high- $T_N$  AF1 layer. In 5/1 bilayer, the  $T_N$  of the AF2 layer is nearly identical to that of the whole bilayer. This indicates that the high- $T_N$  AF1 layer significantly affects the  $T_N$  of the AF2 layer. As the thickness of the AF2 layer increases (as one moves from 5/1 to 5/7 bilayer), the  $T_N$  of the AF2 layer reduces in comparison to the bilayer, specifically for higher values of  $U_2$ . The  $T_N$  of the AF2 layer in the 5/7 bilayer prominently exhibits nonmonotonic behavior with  $U_2$ , similar to the bulk system. The inset of (a) displays the bulk system's  $T_N$  vs  $U$ . Here, PM-M (PM-I) represents paramagnetic metal (paramagnetic insulator). AF-I indicates antiferromagnetic insulating state. (d) The variation of  $T_N$  of the AF2 layer with  $U_2$  for various bilayers is shown for comparison. For thicker AF2 layers (i.e., for 5/9 and 5/11 bilayers), the AF2 layer's  $T_N$  approaches the bulk  $T_N$  at high  $U_2$  values. To better visualize this characteristic, we re-plotted the  $T_N$  of the bulk system for different  $U_2$  using the black dashed line.

the whole bilayer system. The Neel temperatures of the 5/1 bilayer remain steady across all  $U_2$  values and are comparable to the AF1 system. It's interesting to note that for all  $U_2$  values, the  $T_N$  of the AF2 layer and the  $T_N$  of the 5/1 bilayer are equal barring  $U_2 = 2$  and 20 values. Thus, the high- $T_N$  AF1 layer in the 5/1 bilayer greatly raises the  $T_N$  of the AF2 layer.

For the 5/3 bilayer, the  $T_N$  of the AF2 layer reduces slightly for  $U_2 > 8$ , as seen in Fig. 2(b). However, the AF2 layer has a higher  $T_N$  than the corresponding bulk system for any specified  $U_2$ , but is lower than the bilayer's  $T_N$  value (unless  $U_2 = U_1 = 8$ ). The  $T_N$  of the AF2 layer exhibits nonmonotonic behavior with  $U_2$  for the 5/7 bilayer, as shown in Fig. 2(c), similar to bulk systems [see in set of Fig. 2(a)]. Clearly, the  $T_N$  of the AF2 layer is less than that of the bilayer system. The  $T_N$  of the AF2 layer in the bilayer decreases with increasing the thicknesses, as shown in Fig. 2(d). The reduction is particularly noticeable for higher values of  $U_2$ . The  $T_N$  of

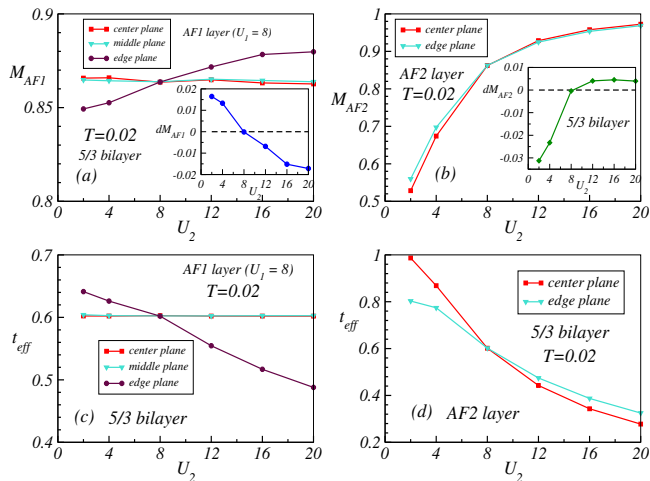


FIG. 3: (a) The local moment in the edge, middle, and center planes of the AF1 layer ( $U_1 = 8$ ) of a 5/3 bilayer is plotted with varying  $U_2$  value in the AF2 layer at  $T = 0.02$ . When  $U_2 < 8$  ( $U_2 > 8$ ), the local moment in the edge plane of the AF1 layer is smaller (larger) than in the center plane. The inset shows the  $dM_{AF1}$ , which is the difference in average local moment between the AF1 layer's center and edge planes.  $dM_{AF1}$  is positive (negative) when  $U_2 < 8$  ( $U_2 > 8$ ). (b) At  $T = 0.02$ , the local moments in both edge and center planes of AF2 layer increase monotonically as  $U_2$  increases. The local moment in the edge plane of the AF2 layer is larger (marginally smaller) than the center plane for  $U_2 < 8$  ( $U_2 > 8$ ). The inset shows the  $dM_{AF2}$ , which represents the difference in local moment between the AF2 layer's center and edge planes. For  $U_2 < 8$ ,  $dM_{AF2}$  is negative, but for  $U_2 > 8$ , it's positive. (c) The  $t_{eff}$  in the edge plane of the AF1 layer decreases as the  $U_2$  of the AF2 layer increases, whereas the  $t_{eff}$  in the middle and center planes remains nearly constant. (d) As  $U_2$  increases in the AF2 layer, the  $t_{eff}$  in both the edge and center planes decreases. Interestingly, the edge plane has a larger (smaller)  $t_{eff}$  than the center plane for  $U_2 < 8$  ( $U_2 > 8$ ) in AF1 layer whereas  $t_{eff}$  of the edge plane is smaller (larger) in AF2 layer for  $U_2 < 8$  ( $U_2 > 8$ ) due to interfacial coupling.

the AF2 layer closely resembles that of the bulk system for thicker AF2 layers (such as in 5/9 and 5/11 bilayers) and larger  $U_2$  values, suggesting that the proximity effect is reduced to affect the inner AF2 layers as AF2 layer's thickness increases.

To further investigate the proximity effect, we plot the magnetic moment profiles of the 5/3 bilayer system as shown in Fig. 3(a). The 5/3 bilayer that we choose for this investigation contains two edge planes, two middle planes, and one center plane in the AF1 layer and two edge planes and one center plane in the AF2 layer [see Fig. 1]. This provides a platform to estimate the range of the interfacial effect, i.e., how far AF1 layer affects the AF2 layer and vice versa. In Figs. 3(a) and (b), we show the moment profiles of the constituent planes of the AF1 and AF2 layers, respectively at  $T = 0.02$  by varying the strength of Coulomb repulsion  $U_2$  of the AF2 layer. In the center plane of the AF1 layer, the magnetic mo-

ment stays almost constant and near the bulk limit for  $U_1 = 8$  [see Fig. 3(a)]. Additionally, the magnetic moment in the middle planes follows the center plane and does not fluctuate significantly. But, the presence of AF2 layer modifies the magnetic moment in the AF1 layer's edge planes. For  $U_2 < 8$  ( $U_2 > 8$ ), the average moment of the AF1 layer's edge planes is smaller (greater) than that of the layer's center plane. For visual clarity, we have displayed  $dM_{AF1}$  ( $= M_{AF1}^{center} - M_{AF1}^{edge}$ ) in the inset of Fig. 3(a) to illustrate the crossover of  $dM_{AF1}$  from positive to negative at  $U_2 = U_1 = 8$ . On the other hand, the AF2 layer's center plane and edge plane moments grow monotonically as  $U_2$  increases and saturate at higher  $U_2$  values (see Fig. 3(b)) similar to the bulk calculations<sup>63,75</sup>. Unlike the AF1 layer, the average moment in the edge plane is bigger (smaller) than the center plane for  $U_2 < 8$  ( $U_2 > 8$ ). However, the difference is very small for  $U_2 > 8$ . The negative to positive crossover of  $dM_{AF2}$  ( $= M_{AF2}^{center} - M_{AF2}^{edge}$ ) is shown in the inset of Fig. 3(b).

It is highly likely that the coupling between antiferromagnetic layers at the interface in AF1/AF2 bilayers alters the magnetic moment profiles of edge planes. To investigate this correspondence, we evaluate the effective hopping  $t_{eff}$  for the various planes of the AF1 and AF2 layers, as illustrated in Figs. 3(c) and (d), respectively, for 5/3 bilayer at  $T = 0.02$ . The  $t_{eff}$  values remain constant in the center and middle planes of the AF1 layer as we increase  $U_2$  values and the obtained values are closer to the bulk limit for  $U_1 = U = 8$  [see Fig. 3(c)]. This indicates that the moment profile of central planes remains more or less unaffected.

The  $t_{eff}$  in both edge and center planes of the AF2 layer decreases monotonically with increasing  $U_2$  values as shown in Fig. 3(d). This pattern indicates that moments are becoming increasingly localized with increasing  $U_2$ . This decrease in  $t_{eff}$  value with increasing  $U_2$  has a significant impact on the edge plane of the AF1 layer as shown in Fig. 3(c). Unlike the AF1 layer, the  $t_{eff}$  of the edge plane of the AF2 layer is smaller (bigger) than that of the center plane for  $U_2 < 8$  ( $U_2 > 8$ ). As a result, for  $U_2 < 8$  ( $U_2 > 8$ ), the moments in the edge plane of AF2 layer become more (less) localized than the center plane when the AF2 layer makes contact with the AF1 layer. Overall, the  $t_{eff}$  and  $M$  calculations shown in Fig. 3, corroborate each other very nicely.

## V. MAGNETOTRANSPORT PROPERTIES OF AF1(HIGH- $T_N$ )/AF2(LOW- $T_N$ ) BILAYERS [ $U_1 = 8$ AND $U_2 = 16$ ]

Now, we study the AF1/AF2 bilayers in details by assigning  $U_2 = 2 \times U_1$ , for which  $T_N$  of both AF1 and AF2 are clearly distinct. For  $U_1 = 8$ , the  $T_N$  of corresponding bulk system is 0.21, with a magnetic moment  $M$  of roughly 0.86. For  $U_2 = 16$ , the corresponding bulk system has a lower  $T_N$  ( $= 0.12$ ) and a magnetic moment  $M$  of approximately  $M \sim 0.95$ . In our calculations, we

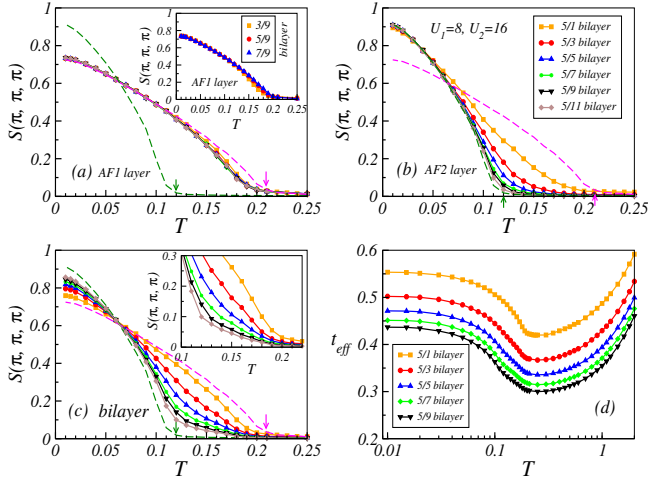


FIG. 4:  $S(\pi, \pi, \pi)$  vs  $T$  across various layers: (a) the AF1 layer, (b) the AF2 layer, and (c) the whole bilayer. Thickness of AF1 layer is set at  $w_1 = 5$ , whereas the AF2 layer's thickness varies from  $w_2 = 1$  to 11. The magenta and green dashed lines are used to plot the  $S(\pi, \pi, \pi)$  vs  $T$  of bulk systems corresponding to  $U_1 = 8$  and  $U_2 = 16$ , respectively. The magenta and green arrows represent the  $T_N$ s of the bulk systems. The  $T_N$  of the AF1 layers remains same for all the bilayers. The inset of (a) displays the temperature dependence of  $S(\pi, \pi, \pi)$  of the AF1 layer in 3/9, 5/9, and 7/9 bilayers. Inset also shows that the  $T_N$  of the AF1 layers remains intact when we fix  $w_2 = 9$  and vary  $w_1$ . However, the  $T_N$  of the AF2 layer decreases as its thickness increases. Interestingly, the  $T_N$  of the entire bilayer stays more or less constant. The inset of (c) displays an enlarged view of the structure factors of the whole bilayers close to the transition temperature. In (a)-(c), legends are the same. (d) The temperature evolution of  $t_{eff}$  for different bilayers is displayed. The dip points in  $t_{eff}$ , which represent the antiferromagnetic transition, are the same for each bilayer. As the thickness of the AF2 layer varies, this reiterates that the  $T_N$  of the whole bilayer remains unchanged. Throughout all calculations,  $U_1$  (associated with the AF1 layer) and  $U_2$  (linked to the AF2 layer) are set at  $U_1 = 8$  and  $U_2 = 16$ .

classify AF1 (with  $U_1 = 8$ ) and AF2 (with  $U_2 = 16$ ) layers as high- $T_N$  and low- $T_N$  antiferromagnetic layers, respectively. The parameter selection reflects the qualitative characteristics of antiferromagnetic layers in well-studied NiO/CoO bilayers, including higher  $T_N$  for NiO and higher magnetic moment for CoO<sup>33-35,40,41</sup>. In addition, these  $U$  values comply with those calculated in density functional theory calculations for NiO<sup>78-82</sup> and CoO<sup>83,84</sup>. So, we choose these two  $U$  values to demonstrate the enhancement of Neel temperature of a low- $T_N$  antiferromagnet in contact with a high- $T_N$  antiferromagnet, as observed in NiO/CoO bilayers<sup>33-35,40,41</sup>. It is important to note here that our calculations for mimicking NiO or CoO are qualitative in nature.

The magnetic properties of AF1/AF2 bilayers are analyzed by calculating the antiferromagnetic structure factors  $S(\pi, \pi, \pi)$  for the layers and the planes, as well as the total bilayer. Temperature-dependent structure fac-

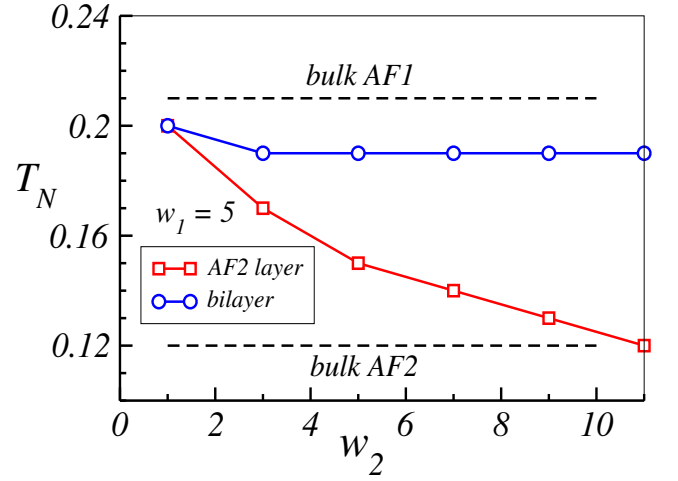


FIG. 5: The Neel temperature  $T_N$  of the AF2 layer and the whole bilayer is displayed for various AF2 layer thicknesses. While the  $T_N$  of the AF2 layer decreases as its thickness increases, the  $T_N$  of the bilayer remains more or less constant. The black dashed lines represent the  $T_N$ s of the bulk systems corresponding to the AF1 ( $U_1 = 8$ ) and AF2 ( $U_2 = 16$ ) layers as indicated in the figure.

tors  $S(\pi, \pi, \pi)$  for bilayers and individual layers by changing the thickness of the AF2 layer ( $w_2$ ) while keeping the thickness of the AF1 layer constant at  $w_1 = 5$  are shown in Fig. 4. The  $T_N$  of the AF1 layer stays stable at  $T \sim 0.2$  in all bilayer systems investigated in this work as shown in Fig. 4(a). The  $T_N$  of the AF1 layer also remains constant when the thickness of the AF1 layer ( $w_1$ ) is modified, but the thickness of the AF2 layer is fixed, as illustrated in the inset. On the other hand,  $T_N$  of the AF2 layer decreases as the thickness  $w_2$  increases, approaching the bulk limit at  $w_2 = 11$  [see Fig. 4(b)]. Interestingly, as the thickness of the AF2 layer increases, the bilayer's  $T_N$  remains relatively constant due to the influence of the AF1 layer [see Fig. 4(c)]. The zoomed version around  $T_N$  is plotted in the inset. We also ascertain the  $T_N$  by calculating the effective hopping parameter  $t_{eff}$  of the bilayers. The localization of moments causes a decrease in  $t_{eff}$  as the temperature decreases. It then starts increasing at  $T_N$  due to delocalization of moments supported by virtual hopping, which establishes the onset of the antiferromagnetic ordering. A dip in  $t_{eff}$  around  $T = 0.2$  as shown for different bilayers in Fig. 4(d) helps us to double check the  $T_N$  values.

Fig. 5 summarizes the systematics of the  $T_N$ . The black dashed lines represent the  $T_N$ s of the bulk systems corresponding to the AF1 ( $U_1 = 8$ ) and AF2 ( $U_2 = 16$ ) layers. Overall, our calculations show that the  $T_N$  of the AF2 layer decreases with increasing the thicknesses of the AF2 layer in the AF1/AF2 bilayer system. So, the  $T_N$  of the low- $T_N$  AF2 layer increases significantly at smaller thicknesses, whereas at larger thicknesses, it approaches the value of the bulk system.

Additionally, for better visualization, we plot the

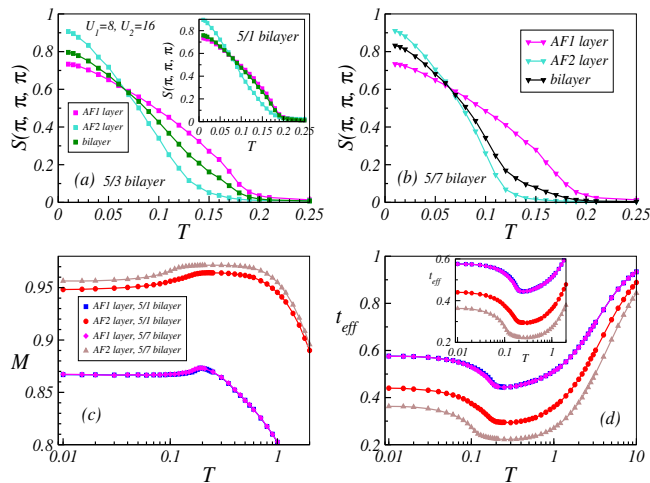


FIG. 6: Layer-resolved magnetic properties: Temperature variation of the structure factor  $S(\pi, \pi, \pi)$  of AF1 and AF2 layers along with the total bilayer are shown for (a) the 5/3 bilayer and (b) the 5/7 bilayer. The  $T_N$  of the AF2 layer in 5/3 bilayer is enhanced whereas the  $T_N$  of the AF2 layer in 5/7 bilayer approaches its bulk limit. Inset of (a) demonstrates that the  $S(\pi, \pi, \pi)$  of the AF1 and AF2 layers as well as the total 5/1 bilayer exhibit same  $T_N$ . (c) Temperature evolution of the local moment  $M$  of the AF1 and AF2 layers is plotted for the 5/1 and 5/7 bilayers. A little decrease in moment is observed for the AF2 layer in the 5/7 bilayer at a lower temperature (see range  $T = 0.1 - 0.2$ ) compared to the temperature for the AF2 layer in the 5/1 bilayer. This indicates that the AF2 layer's  $T_N$  in the 5/7 layer is less than that of the 5/1 bilayer. For more details please see the texts. (d) For the 5/1 and 5/7 bilayers, the temperature evolution of  $t_{eff}$  of the constituent AF1 and AF2 layers is displayed. The low temperature upturn in  $t_{eff}$  of the AF2 layer, which is associated with Neel temperature, is situated lower temperature in the 5/7 bilayer than in the 5/1 bilayer. The inset shows a zoomed version of the same in (c) and (d), legends are same. All the calculations are performed for  $U_1 = 8$  and  $U_2 = 16$ .

$S(\pi, \pi, \pi)$  vs  $T$  for the individual AF1 and AF2 layers alongside their associated bilayers in Fig. 6(a) and Fig. 6(b) for 5/3 and 5/7 bilayer, respectively. In the inset of Fig. 6(a), we illustrate the  $T_N$  of the AF1 and AF2 layers for 5/1 bilayer system, where the  $T_N$  of the AF2 layer closely matches that of the AF1 layer. In 5/3 bilayer, the  $T_N$  of AF1 and AF2 layers differ significantly, while the  $T_N$  of the AF2 layer stays higher than that of the bulk counterpart. Hence, the proximity of the high- $T_N$  antiferromagnet in the bilayers enhances its  $T_N$ , particularly for thinner AF2 layers, similar with experiments<sup>33-35,40,41</sup>. For 5/7 bilayers, the bifurcation between  $T_N$  of AF1 and AF2 layers is apparent more clearly. The  $T_N$  of the AF2 layer in 5/7 bilayer is close to the bulk value  $T_N \sim 0.12$  and for the bilayer that has thicker AF2 layer (e.g.  $w_2 = 11$ ), the  $T_N$  of the AF2 layer matches to its bulk limit [see Fig. 4(b)]. Therefore, it is obvious that the proximity effect of the AF1 layer has a considerable impact on the  $T_N$  of the AF2 layer up

to  $w_2 = 9$ .

Furthermore, we show the moment profiles of the individual AF1 and AF2 layers for the 5/1 and 5/7 bilayers in Fig. 6(c) in order to obtain additional evidence of the thickness dependency of the  $T_N$ . It is well known that the bulk system exhibits a tiny peak around transition temperatures as a result of moment delocalization aided by virtual hopping assisted by the antiferromagnetic correlations<sup>64</sup>. The magnetic moment profile of the AF1 layers also shows a peak around  $T = 0.2$  that is similar to bulk systems. The AF1 layer's peak location in the 5/1 bilayer and the 5/7 bilayer overlap with each other. As previously presented in Fig. 4(a), this also suggests that the resulting  $T_N$  of the AF1 layer in 5/1 and 5/7 bilayers are equal to each other. While the AF2 layer's peak structure is not very apparent, the antiferromagnetic transition is indicated by a modest drop in moment between  $T = 0.2$  and 0.1. As we move from the 5/1 to the 5/7 layer, the temperature at which this drop is observed decreases, indicating that the  $T_N$  of the AF2 layer in the 5/7 bilayer is lower than that in the 5/1 bilayer.

In addition, we evaluate the effective hopping parameter  $t_{eff}$  of AF1 and AF2 layers for 5/1 and 5/7 bilayers to ascertain the antiferromagnetic transitions. First, as previously stated, the temperature at which the AF1 layers' dip in  $t_{eff}$  appears corresponds to their magnetic transition and comes as equal to  $T_N$ . Secondly, the dip for AF1 and AF2 layers occurs at the same temperature for 5/1 bilayers as shown in Fig. 6(d), but differs for 5/7 layers. This demonstrates that the  $T_N$  of AF1 and AF2 layers (in 5/7 layers) are distinct from one another. Consequently, the AF2 layer's  $T_N$  in the 5/7 bilayer is less than that in the 5/1 bilayer.

We also calculate the specific heat  $C_v$ , as shown in Fig. 7(a), in order to understand the systematics of the transition temperatures of the bilayers with change of the thicknesses of the AF2 layers. To get an idea about the transition temperatures, we examine the specific heat up to  $T = 0.5$ . There is a noticeable single-peak structure in the specific heat for 5/1 bilayer. This single-peak structure suggests that the whole system experiences antiferromagnetic transition at a particular temperature. This result also confirms that the  $T_N$  of AF1 and AF2 layers are equal to each other in 5/1 bilayer. Conversely, the 5/7 bilayer exhibits two-peak features because to its thick AF2 layer. One of the two peaks (peak at relatively higher temperature) is linked to the AF1 layer's antiferromagnetic ordering, while the other is connected to the AF2 layer's antiferromagnetic transition. Therefore, for higher (lower) thicknesses of the AF2 layers in the bilayers, the two-peak (one-peak) character of the specific heat is compatible with the systematics of the structure factors as shown in Fig. 6.

In order to substantiate the two-peak structure of specific heat, we vary the thicknesses of AF2 layer as shown in Fig. 7(b). As we mentioned above the single peak around  $T = 0.2$  is associated with  $T_N$  of both AF1 and AF2 layers for 5/1 bilayer. For 5/3 bilayer another broad



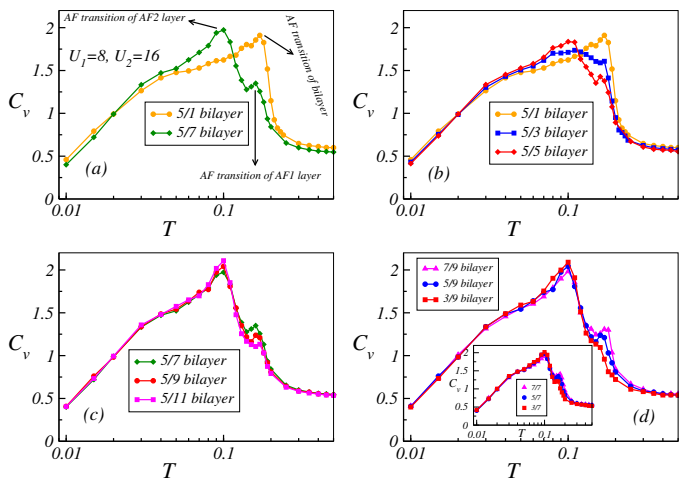


FIG. 7: a) Temperature dependence of specific heat  $C_v$  for the 5/1 and 5/7 bilayers. The specific heat curve of the 5/1 (5/7) bilayer exhibits a single-peak (double-peak) structure. A single peak in the 5/1 bilayer implies that the magnetic transition points for the AF1 and AF2 layers are the same. One peak out of two peaks for the 5/7 bilayer (in particular, the peak at relatively high temperature) is associated with the AF1 layer’s antiferromagnetic transition, while the other is associated with the AF2 layer’s antiferromagnetic transition. Black arrows point to these peaks. (b) Temperature dependency of  $C_v$  in 5/1, 5/3, and 5/5 bilayers is analyzed to identify systematic variations as AF2 layer thickness varies. (c) The specific heat  $C_v$  is plotted as a function of temperature for the 5/7, 5/9, and 5/11 bilayers. As the thickness  $w_2$  of the AF2 layer increases, the peak associated with the magnetic transition of the AF1 layer is suppressed. In (d) specific heat variations of 3/9, 5/9, and 7/9 bilayers with temperature are compared. Here, the thickness of the AF1 layer  $w_1$  varies from 3 to 9, while the thickness of the AF2 layer set at  $w_2 = 9$ . The inset in (d) shows the  $C_v$  vs  $T$  for the 3/7, 5/7, and 7/7 bilayers (i.e., with a fixed AF2 layer thickness of  $w_2 = 7$  and variable AF1 layer thicknesses). The magnitude of the peak linked to the AF1 layer decreases as its thickness  $w_1$  decreases.

peak emerges just below  $T = 0.2$  that is related to the onset of magnetization in the AF2 layer which differs from  $T_N$  of the AF1 layer characterized by the peak around  $T = 0.2$ . This second peak is more prominent for 5/5 bilayer. At the same time, the peak height associated with the AF1 layer decreases with increasing the thicknesses of the AF2 layers. This trend is also clearly visible as we move from 5/7 to 5/11 bilayer [see Fig. 7(c)].

On the other hand, for a fixed thickness of the AF2 layer, e.g.,  $w_2 = 9$  [see Fig. 7(d)] or  $w_2 = 7$  [see inset of Fig. 7(d)], the peak height associated with the AF1 layer decreases as the thickness of the AF1 layer decreases from  $w_1 = 7$  to 3, while the peak height associated with the AF2 layer remains more or less unaffected. In fact, the peak in the specific heat associated with the antiferromagnetic ordering of the AF1 layer is not prominent for the 3/9 bilayer [see Fig. 7(d)]. But, the antiferromagnetic transition is inherent in the AF1 layer of 3/9 bilayer like

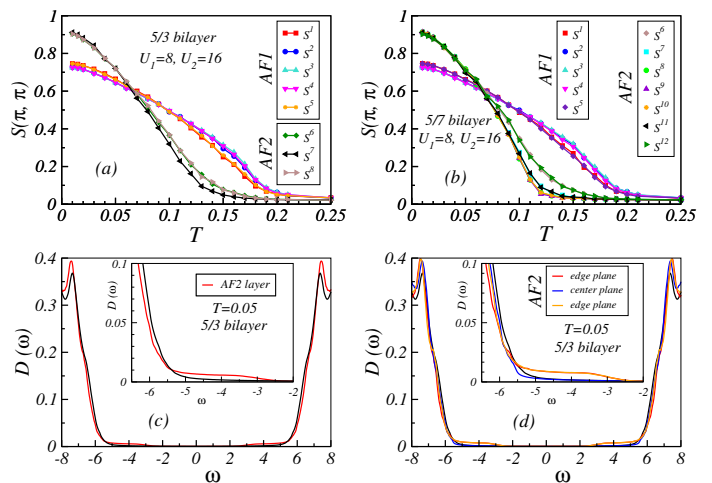


FIG. 8: Temperature-dependent structure factor  $S(\pi, \pi)$  for individual planes in (a) 5/3 and (b) 5/7 bilayers. Antiferromagnetic transitions occur at  $T \sim 0.2$ , according to  $S(\pi, \pi)$  vs.  $T$  plots for all the planes in the AF1 layer (i.e. for  $S^1, S^2, S^3, S^4,$  and  $S^5$  planes) for both the bilayers. The  $T_N$  of the edge planes ( $S^6$  or  $S^8$ ) of the AF2 layer in the 5/3 bilayer is greater than that of the center plane ( $S^7$ ). In 5/7 bilayer, as one moves deeper into the AF2 layer from the interfaces (i.e., from  $S^6$  to  $S^9$ ), the  $T_N$  decreases. The  $S(\pi, \pi)$  of all the inner planes ( $S^8, S^9,$  and  $S^{10}$ ) exhibit antiferromagnetic transitions approximately at  $T \sim 0.12$ , which is equivalent to the  $T_N$  of the AF2 layer in its bulk limit. (c) The density of states (DOS) of the AF2 layer of the 5/3 bilayer is displayed at  $T = 0.05$ . The inset re-plots a zoomed-in version of the DOS close to the gap’s boundary. (d) At  $T = 0.05$ , the DOS of the AF2 layer’s two edge planes and one center plane are displayed separately. The edge planes show finite although very small finite DOS at the boundaries of the gap. Inset: The DOS close to a gap boundary is also re-plotted in a zoomed-in version. For comparison, the DOS of the bulk system for  $U_2 = 16$  is also plotted at  $T = 0.05$  by a black line in (c) and (d).

the AF1 layer in the 5/9 and 7/9 bilayers, as confirmed from the structure factor calculations shown in the inset of Fig. 4(a). Overall, for larger thicknesses of the AF2 layer, the specific heat of the bilayers exhibits two-peak characteristics, consistent with the experimental observations.

We also explore the plane-resolved antiferromagnetic structure factors to better understand how the AF2 layer’s Neel temperature is enhanced. Figs. 8(a) and 8(b) show plots of  $S(\pi, \pi)$  for all planes of the 5/3 and 5/7 bilayers, respectively. The high- $T_N$  AF1 layer’s constituent planes undergo antiferromagnetic transitions at the same temperature,  $T \sim 0.2$ , for both the 5/3 and 5/7 bilayers. The edge planes of low- $T_N$  AF2 layer in 5/3 bilayer display a higher Neel temperature than the center plane.  $S^6$  and  $S^8$  represent the edge planes of the AF2 layer as indicated in Fig. 8(a). Nonetheless, the center plane ( $S^7$  plane) has an enhanced Neel temperature than the  $T_N$  of AF2 layer at the bulk limit.

The inner planes of the AF2 layer in the 5/7 layer [ $S^8$ ,  $S^9$ , and  $S^{10}$  planes in Fig. 8(b)] exhibit antiferromagnetic transitions at the same temperature, i.e. at 0.12, which corresponds to the  $T_N$  of the low- $T_N$  AF2 layer in the bulk limit. But, the  $T_N$  of edge planes [see  $S^6$  and  $S^{12}$  planes in Fig. 8(b)] are truly enhanced, while planes just next to the edge plane [see  $S^7$  and  $S^{11}$  plots in Fig. 8(b)] are marginally augmented as compared to inner planes. As the thickness of the AF2 layer increases, the proximity effect is limited to its interfacial planes. It increases the Neel temperature of the edge plane while leaving the inner individual planes unchanged. So, the  $T_N$  decreases as one advances deeper planes into the AF2 layer from the interface, eventually approaching the bulk limit for the inner planes.

We calculate the density of states (DOS) to emphasize the fact that the edge planes are more influenced. First, we plot the DOS of the AF2 layer for the 5/3 bilayer at  $T = 0.05$  in Fig. 8(c). Additionally, we plot the DOS of the corresponding bulk system for  $U_2 = 16$ . Like the bulk system, the AF2 layer's DOS exhibits a pronounced Mott-gap. The main difference is that, for the AF2 layer, a small finite DOS is visible at the gap's boundaries [see the inset of a zoomed version]. To determine which planes of the AF2 layer are responsible for generating finite DOS on the end of the gap, we examine the DOS of every single plane of the AF2 layer, as shown in Fig. 8(d). The DOS of the center plane roughly reciprocate with the DOS of the corresponding bulk system. However, the AF2 layer's edge planes show finite DOS at the gap's boundaries. This change in the DOS of the AF2 layer's edge planes results from the coupling of the AF2 layer with the AF1 layer at the interfaces, which is driven by delocalization of moments across the interfaces.

In order to ascertain the extent to which the AF1 layer affects the AF2 layer regarding the delocalization of moments across the interface, we calculate the  $t_{eff}$  values of the various planes for the 5/3 and 5/7 bilayers. For the 5/3 bilayer, the temperature-dependent  $t_{eff}$  value [see Fig. 9(a)] indicates that all the planes undergo a magnetic transition as discussed in Fig. 9(d). It also demonstrates that  $t_{eff}$  in the edge planes are bigger (smaller) than the center plane in both AF2 (AF1) layers.

We extract the  $t_{eff}$  vs. plane index  $i$  for the 5/3 bilayer at low temperatures  $T = 0.05$  and 0.02 and plot those in Fig. 9(b) to present a clear picture. The same data are provided for the 5/7 bilayer as well in Fig. 9(c). Because of coupling with the strongly localized AF2 layer ( $U_2 = 16$ ) at the interfaces, it is evident that at any given temperature, the  $t_{eff}$  in the AF1 layer's edge planes is less than the middle and center planes. On the other hand, because of the coupling with the relatively delocalized AF1 layer, the  $t_{eff}$  in the AF2 layer's edge planes is greater than the center plane. In other words, in the AF2 (AF1) layer, the moments in the edge plane become more (less) delocalized than those in the center plane. The enhancement of the  $T_N$  of AF2 layer results from this delocalization-driven interaction of the edge planes

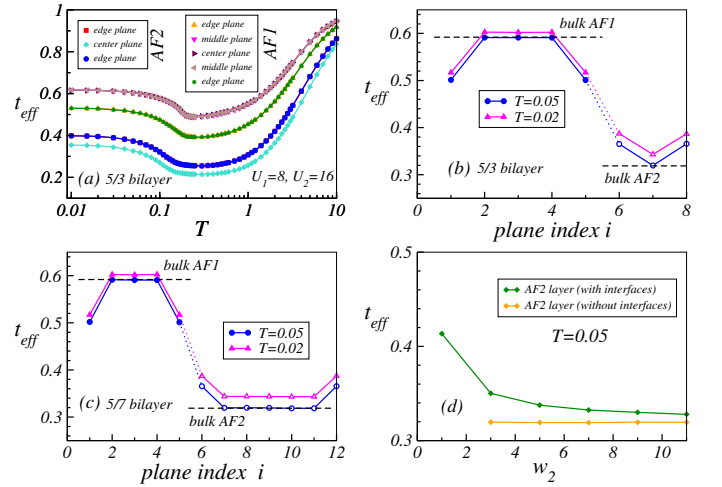


FIG. 9: For the 5/3 bilayer, the temperature evolution of the  $t_{eff}$  of the two edge planes, two middle planes, and one center plane of the AF1 layer and the two edge planes and one center plane of the AF2 layer is displayed. The AF1 (AF2) layer's edge planes have a smaller (bigger)  $t_{eff}$  than the center plane.  $t_{eff}$  is plotted against the plane index  $i$  for (b) 5/3 bilayer and (c) 5/7 bilayer at  $T = 0.05$  and 0.02. The planes of the AF1 (AF2) layer are represented by the solid (open) symbol. The coloured dotted line shows the link between the interfacial planes. The black dashed line represents the  $t_{eff}$  of the bulk systems corresponding to AF1 ( $U_1 = 8$ ) and AF2 ( $U_2 = 16$ ) layers at  $T = 0.05$ . This indicates that the inner plane  $t_{eff}$  values of the AF1 and AF2 layers are equal to those of the respective bulk systems. (d) The average value of the  $t_{eff}$  in the AF2 layer (with or without interfacial planes) is depicted at  $T = 0.05$ . As the AF2 layer thickness increases, the  $t_{eff}$  value decreases. However, except for the interfacial planes, the  $t_{eff}$  remains constant.

of the AF2 layer with the AF1 layer.

It's also interesting to note that while the average  $t_{eff}$  in the AF2 layer excluding the interfacial planes stays constant during the thickness variation of AF2 layer, the average  $t_{eff}$  of all the planes in the AF2 layer falls as its thickness increases [see Fig. 9(d)]. According to all of these results, the AF1 layer's delocalization-induced influence on the AF2 layer decreases as the AF2 layer's thickness increases and proximity effect mostly stays confined at the interfacial edge planes.

## VI. MAGNETOTRANSPORT PROPERTIES OF (HIGH- $T_N$ -AF)/(LOW- $T_N$ -AF) BILAYERS [ $U_1 = 8$ AND $U_2 = 4$ ]

In previous section we explored the (high- $T_N$  AF1)/(low- $T_N$  AF2) bilayers by assigning  $U_1 = 8$  to the AF1 layer and  $U_2 = 16$  to the AF2 layer, i.e., for the  $U_2 = 2 \times U_1$  scenario. For the  $U_2 = 0.5 \times U_1$  case, we select  $U_2 = 4$  with a bulk  $T_N$  of 0.14. This ensures that the AF2 layer acts as a low- $T_N$  antiferromagnet. So, in this section we investigate the magnetic and transport

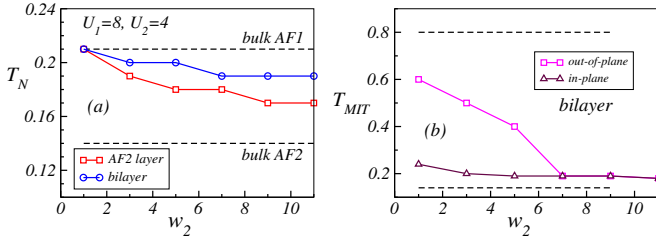


FIG. 10: The  $T_N$  of the AF2 layer and the whole bilayer are shown by varying the thicknesses of AF2 layer. The  $T_N$  of AF1 ( $U_1 = 8$ ) and AF2 ( $U_2 = 4$ ) layers in their bulk limit are represented by the black dashed lines as indicated in the figure. The  $T_N$  profile clearly shows that the  $T_N$  of the AF2 layer in AF1/AF2 bilayer is greater than that of the corresponding bulk system. (b) The  $T_{MIT}$ s of bilayers are plotted with varying AF2 layer thicknesses. The  $T_{MIT}$  is determined by the temperature variations of the in-plane and out-of-plane resistivities. The top (bottom) dashed line represents the  $T_{MIT}$  of the bulk system corresponding to the AF1 (AF2) layer.  $U_1$  (associated with the AF1 layer) and  $U_2$  (related with the AF2 layer) are fixed at  $U_1 = 8$ ,  $U_2 = 4$  throughout the calculations.

properties of another set of high- $T_N$ /low- $T_N$  (AF1/AF2) bilayers and compare them to prior section results as needed. Unlike the previous case, the moments in the AF2 layer are more delocalized than in the AF1 layer. Thus, it will be interesting to find out how the  $T_N$  of the AF2 layer is impacted by the localized moments in the AF1 layer. In our calculations, we modify the thickness of the AF2 layer while keeping the thickness of the AF1 layer fixed at  $w_1 = 5$ , just like we studied in the previous section.

In Fig. 10(a), we show how the  $T_N$  of AF1/AF2 bilayer systems varies by altering the thickness of the low- $T_N$  AF2 layer while keeping the thickness of the high- $T_N$  AF1 layer constant at  $w_1 = 5$ . The bilayer's  $T_N$  decreases slightly as the thickness of the AF2 layer increases. In the 5/1 and 5/3 bilayers (i.e., for  $w_2 = 1$  and 3), the low- $T_N$  AF2 layer's  $T_N$  is significantly enhanced and approaches that of the high- $T_N$  AF1 layer. Interestingly, the  $T_N$  of the AF2 layer in the bilayer diminishes slowly as its thickness increases. This in contrast with the rapid decrease in  $T_N$  for the AF2 layer when  $U_2 = 16$  was used. So, our calculations show that the value of  $T_N$  of AF2 layer is higher than that of the similar bulk system with  $U_2 = 4$ .

Next, we show the metal-insulator transition temperature ( $T_{MIT}$ ) of bilayer systems in Fig. 10(b). As the thickness of the AF2 layer increases, the  $T_{MIT}$  obtained from evaluating the resistivity in out-of-plane direction decreases. The  $T_{MIT}$  ranges from 0.8 to 0.14, representing the corresponding bulk systems with  $U_1 = 8$  and  $U_2 = 4$ , respectively. The range is illustrated by two dashed lines in Fig. 10(b). Beyond 5/7 bilayers, the  $T_{MIT}$  equals  $T_N$ , but for other bilayers (5/1, 5/3, and 5/5),  $T_{MIT}$  exceeds  $T_N$ . In-plane resistivity calculations show that increasing the thickness of the AF2 layer has little effect on  $T_{MIT}$ , except for the 5/1 bilayer with a

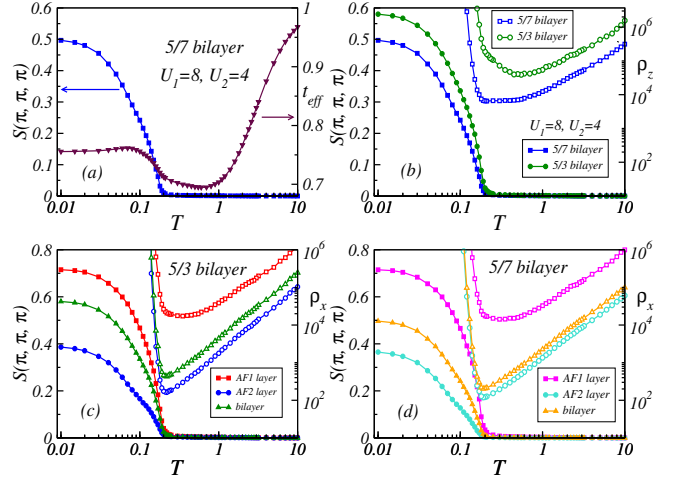


FIG. 11: (a) The temperature evolution of  $t_{eff}$  and  $S(\pi, \pi, \pi)$  are shown for 5/7 bilayer. The  $T_N$  is correlated with the  $t_{eff}$  showing an upturn around  $T = 0.2$ . See text for details. (b) The temperature dependence of  $S(\pi, \pi, \pi)$  and out-of-plane resistivity  $\rho_z$  are plotted for the 5/7 and 5/3 bilayers. The 5/7 bilayer has a slightly smaller  $T_N$  than the 5/3 bilayer. While the 5/3 bilayer's  $T_{MIT}$  is more than its  $T_N$  value, the 5/7 bilayer's  $T_{MIT}$  is equal to its  $T_N$ . Layer-resolved  $S(\pi, \pi, \pi)$  and in-plane resistivity  $\rho_x$  for 5/3 and 5/7 bilayers are plotted in (c) and (d), respectively. To ensure completeness, plots of  $S(\pi, \pi, \pi)$  and  $\rho_x$  for whole bilayers are also shown.

thin AF2 layer.

We present the resistivity data and antiferromagnetic structure factors  $S(\pi, \pi, \pi)$  in Fig. 11 that were utilized to generate the summary shown in Fig. 10. We calculate the temperature dependent  $S(\pi, \pi, \pi)$  and plot it with  $t_{eff}$  of the 5/7 bilayer to ascertain the  $T_N$  in Fig. 11(a). The  $T_N$  from  $S(\pi, \pi, \pi)$  correlates with the  $t_{eff}$ , which shows an upturn around  $T = 0.2$  as temperature decreases. We also plot  $S(\pi, \pi, \pi)$  for 5/3 and 5/7 bilayers in Fig. 11(b) for comparison. The  $T_N$  of the 5/7 bilayer is slightly lower than the 5/3 bilayer but is much larger than the corresponding bulk system for  $U_2 = 4$ . The resistivity calculations in the same figure reveal that the  $T_{MIT}$  of the 5/7 bilayer matches with the  $T_N$ , whereas in the 5/3 bilayer, the  $T_{MIT}$  ( $\sim 0.5$ ) is larger than the  $T_N$ . The fact that the  $T_{MIT}$  of 5/3 bilayer is different from the  $T_N$  suggests that the AF1 layer plays a crucial part in determining the transport in the bilayer when the AF2 layer is thin. It is noteworthy to recall that, in the bulk case for  $U_2 = 4$ , the  $T_{MIT}$  and  $T_N$  are identical, while the  $T_{MIT}$  of the bulk systems corresponding to  $U_1 = 8$  is larger than the  $T_N$ .

For each layer of the 5/3 bilayer, we show temperature dependence of  $S(\pi, \pi, \pi)$  in Fig. 11(c). Additionally, for comparison, we plot the  $S(\pi, \pi, \pi)$  for whole bilayers. The AF2 layer's  $T_N$  ( $\sim 0.19$ ) is marginally less than the AF1 layer's  $T_N$  ( $\sim 0.2$ ). Thus, for  $U_2 = 4$ , the AF2 layer's  $T_N$  is larger than its corresponding bulk  $T_N$ , but it is still somewhat smaller than the  $T_N$  of the AF1

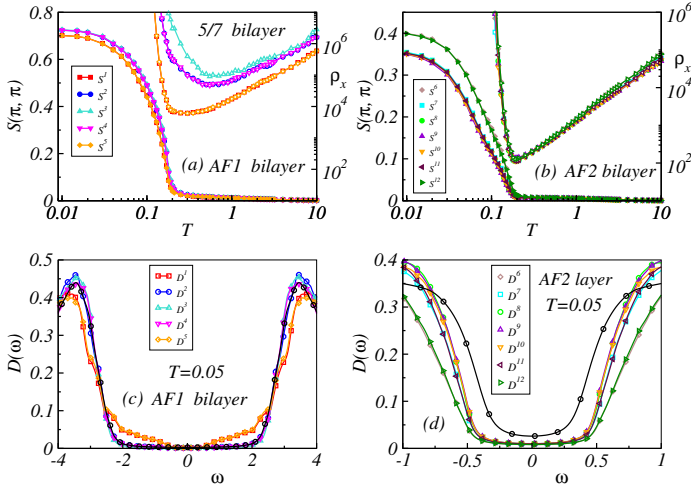


FIG. 12: The temperature evolution of structure factor  $S(\pi, \pi)$  and in-plane resistivity  $\rho_x$  for various planes in the AF1 and AF2 layers of 5/7 bilayer are shown in (a) and (b), respectively. The structure factor (resistivity) curve is indicated by filled (open) symbols. The individual planes of the AF1 layer ( $S^1, S^2, S^3, S^4,$  and  $S^5$ ) exhibit antiferromagnetic transitions at the same temperature,  $T \sim 0.2$ . The  $T_{MIT}$  of the AF1 layer's edge planes is near to  $T_N$ , but for inner planes, it is bigger than  $T_N$ . In the AF2 layer, the  $T_N$  of the edge plane (from  $S^6$  or  $S^{12}$ ) is somewhat higher than that of the inner planes (from  $S^7, S^8, S^9, S^{10}, S^{11}$ ). The resistivities of the AF2 layer's planes are very similar, and the  $T_{MIT}$  matches with the  $T_N$ . For the 5/7 bilayer, the density of states (DOS) of the constituent planes of (c) the AF1 layer and (d) the AF2 layer are shown at  $T = 0.05$ . The DOS of the corresponding bulk system is also plotted for  $U_1 = 8$  in (c) and  $U_2 = 4$  in (d) using a black line. While the DOS in the inner planes ( $D^2, D^3,$  and  $D^4$ ) are extremely close to the bulk limit, the DOS of the AF1 layer's edge plane ( $D^1$  or  $D^5$ ) is modified. The AF2 layer's planes exhibit a wider gap around the Fermi level ( $\epsilon_F = \omega = 0$ ) compared to the bulk system. The edge planes (from  $D^6$  and  $D^{12}$ ) have a somewhat larger gap than the inner planes ( $D^7, D^8, D^9, D^{10},$  and  $D^{11}$ ).

layer. Fig. 11(c) also displays the in-plane resistivities of the AF1 and AF2 layers as well as the entire 5/3 bilayer. The AF2 layer's  $T_{MIT}$  is equal to the AF2 layer's  $T_N$ , while the AF1 layer's  $T_{MIT}$  is greater than the AF1 layer's  $T_N$ . The whole bilayer system exhibits a metal-insulator transition in its in-plane resistivity at the same temperature as the  $T_N$  and  $T_{MIT}$  of AF2 layer. Layer resolved magnetotransport properties of 5/7 bilayer are shown in Fig. 11(d), and the systematics of results are qualitatively similar to those of 5/3 layers.

To get more insight of the proximity effect on the AF2 layer, we examine the plane-resolved magnetotransport properties of the bilayer systems. We show the temperature dependence of  $S(\pi, \pi)$  and in-plane resistivity for each plane of the AF1 layer of the 5/7 bilayer in Fig. 12(a). The constituent planes of the high- $T_N$  AF1 layer undergo antiferromagnetic transitions at roughly the same temperature,  $T \sim 0.2$ . However, compared

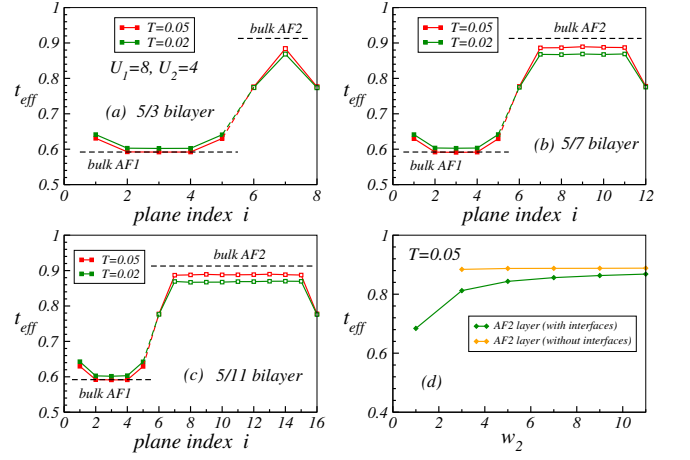


FIG. 13: For the 5/3, 5/7, and 5/11 bilayers the  $t_{eff}$  vs. plane index  $i$  at  $T = 0.05$  and  $0.02$  are plotted in (a), (b), and (c), respectively. The planes of the AF1 (AF2) layer are marked by solid (open) symbols. The colored dashed line indicates the link between the interfacial planes. The black dashed line represents the  $t_{eff}$  of the bulk systems corresponding to  $U_1 = 8$  and  $U_2 = 4$  at  $T = 0.05$ . The  $t_{eff}$  of inner (edge) planes in the AF1 layer is equal to (greater than) the bulk limit. This indicates that the AF1 layer's edge planes are mostly affected in bilayer system. The AF1 layer affects all the planes of the AF2 layer, resulting in smaller  $t_{eff}$  values than the bulk value. However, the AF2 layer's edge planes have smaller  $t_{eff}$  values than the inner planes and are more affected due to interfacial coupling. (d) At  $T = 0.05$ , the average value of  $t_{eff}$  is plotted in the AF2 layer and AF2 layer without interfacial planes. The  $t_{eff}$  in the AF2 layer increases with thickness and reaches saturation at  $w_2 = 9$ . However, except for the interfacial planes, the  $t_{eff}$  of AF2 layer remains constant.

to other planes, the edge plane's  $T_{MIT}$  is much closer to the  $T_N$ . This indicates that the AF1 layer's edge plane is more impacted by the contact with the AF2 layer. Meanwhile, the low- $T_N$  AF2 layer's edge planes show a marginally higher Neel temperature than the center planes.  $S^6$  and  $S^{12}$  represent the edge planes of the AF2 layer as indicated in Fig. 12(b). The Neel temperatures of all inner planes exceed the  $T_N$  of the AF2 layer at the bulk limit. However, there are notable similarities in the temperature dependence of the in-plane resistivity of the different AF2 layer planes, and  $T_{MIT}$  agrees well with the  $T_N$  of the individual AF2 layer planes.

We also plot the plane resolved density of states (DOS) for the AF1 and AF2 layers of the 5/7 bilayer at  $T = 0.05$  in Fig. 12(c) and (d), respectively. For comparison, we include the DOS of the bulk systems corresponding to AF1 ( $U_1 = 8$ ) and AF2 ( $U_2 = 4$ ) layers. The DOS of the interfacial plane away from the Fermi level ( $\epsilon_F = \omega = 0$ ) is somewhat modified as shown in Fig. 12(c). But, the gap around the Fermi level for all the planes is essentially unchanged as compared to the bulk system, according to the plane-resolved DOS of the high- $T_N$  AF1 layer. However, the DOS of all planes in the AF2 layer



shows a larger gap around the Fermi level than the bulk system as illustrated in Fig. 12(d). When the AF2 layer comes into contact with the AF1 layer with a large gap, the proximity effect increases the gap size of the AF2 layer. As expected, proximity to the AF1 layer affects the edge plane of the AF2 layer more than the inner planes.

Next, we plot the  $t_{eff}$  vs. plane index  $i$  for the 5/3 bilayer at low temperatures  $T = 0.05, 0.02$  as shown in Fig. 13(a). The AF1 layer's edge plane has a bigger  $t_{eff}$  than its central (middle and center) planes, suggesting that the moments there become more delocalized upon coming into contact with the AF2 layer. In fact, the AF1 layer's central planes are mostly unaffected, and  $t_{eff}$  is near the comparable bulk value for  $U_1 = 8$ . Conversely, because of the coupling with the more localized AF1 layer, the  $t_{eff}$  in the edge plane of the AF2 layer is smaller than that of the center plane. In the center plane of the AF2 layer, the  $t_{eff}$  is also smaller than the corresponding bulk value of  $U_2 = 4$ .

Additionally, we present the  $t_{eff}$  vs. plane index  $i$  for the 5/7 and 5/11 bilayers at  $T = 0.05, 0.02$  in Fig. 13(b) and Fig. 13(c) respectively. These plots make it clear that all the planes inside the AF2 layer are affected even for larger thicknesses of AF2 layer. However, the moments in edge plane is more prone to localization than the inner planes. The average  $t_{eff}$  in the AF2 layer, excluding interfacial planes, remains constant as the inner planes are equally affected due to the proximity effect of the AF1 layer, as shown in Fig 13(d). But, the average  $t_{eff}$  of the total AF2 layer increases with  $w_2$  (thickness of AF2 layer) and saturates beyond  $w_2 \sim 9$ . These results comprehensively show that the all the planes of AF2 layers are affected although edge plane is more influenced than inner planes. Because of this, the  $T_N$  of the AF2 layer (with  $U_2 = 4$ ) in the bilayer gradually decreases as its thickness increases, in contrast to the results obtained when  $U_2 = 16$  was assigned.

## VII. CONCLUSIONS

In summary, we investigated the magnetotransport properties of the AF1(low- $T_N$ )/AF2(high- $T_N$ ) bilayers

using a one-band Hubbard model at half-filling using semi-classical Monte Carlo approach. In our model Hamiltonian calculations, we set Coulomb repulsion  $U_1 = 8$  to simulate the high- $T_N$  AF1 layer, and  $U_2 = 2 \times U_1$  to simulate the low- $T_N$  AF2 layer. We choose these parameters to mimic NiO/CoO like bilayers. Our calculations indicate that when the thickness of the low- $T_N$  antiferromagnet is small, the proximity effect significantly increases its  $T_N$ , resulting in a single magnetic transition temperature for the bilayer system. A single peak in specific heat corresponds to the bilayer's single-shot antiferromagnetic transition. As the thickness of the AF2 layer increases, its  $T_N$  decreases and approaches the bulk limit, indicating separation from the  $T_N$  of the AF1 layer. The two-peak structure in the specific heat for thicker AF2 layers supports these findings. In particular, we demonstrate that the increase in  $T_N$  of the AF2 layer nevertheless remains an interfacial effect. Overall, our findings qualitatively agree with experimental results and provide insights into the phenomenon of increasing the Neel temperature of low- $T_N$  antiferromagnets in bilayer systems.

We additionally carried out the analysis for  $U_1 = 8$  and  $U_2 = 0.5 \times U_1$  for completeness. Here, the low- $T_N$  antiferromagnet's  $T_N$  is enhanced even for thicker AF2 layers, unlike when  $U_2 = 2 \times U_1$ . Therefore, in the  $U_2 = 0.5 \times U_1$  instance, the proximity effect penetrates to the inner planes due to a comparatively higher delocalization of moments in the AF2 layer. Density of states calculations also show that proximity to the AF1 layer significantly impacts both the interfacial and inner planes of the AF2 layer in this scenario. It would be interesting to conduct experiments on these types of bilayers.

## ACKNOWLEDGMENT

We acknowledge use of the Meghnad2019 computer cluster at SINP.

---

\* Electronic address: [kalpataru.pradhan@saha.ac.in](mailto:kalpataru.pradhan@saha.ac.in)

<sup>1</sup> I. Fina, X. Marti, D. Yi, J. Liu, J. H. Chu, C. Rayan-Serrao, S. Suresha, A. B. Shick, J. Zelezny, T. Jungwirth, J. Fontcuberta, and R. Ramesh, Nat. Commun. **5**, 1 (2014).

<sup>2</sup> X. Marti, I. Fina, C. Frontera, J. Liu, P. Wadley, Q. He, R. J. Paull, J. D. Clarkson, J. Kudrnovsky, I. Turek et al., Nat. Mater. **13**, 367 (2014).

<sup>3</sup> P. Wadley, B. Howells, J. Zelezny, C. Andrews, V. Hills, R. P. Campion, V. Novák, K. Olejník, F. Maccherozzi, S. S. Dhesi et al., Science **351**, 587 (2016).

<sup>4</sup> P. Wadley, S. Reimers, M. J. Grzybowski, C. Andrews, M. Wang, J. S. Chauhan, B. L. Gallagher, R. P. Campion, K. W. Edmonds, S. S. Dhesi et al., Nat. Nanotechnol. **13**, 362 (2018).

<sup>5</sup> S. Mangin, D. Ravelosona, J. A. Katine, M. J. Carey, B. D. Terris, and E. E. Fullerton, Nature Mater. **5**, 210 (2006).

<sup>6</sup> R. Sbiaa, R. Law, S. Y. H. Lua, E. L. Tan, T. Tahmasebi, C. C. Wang, and S. N. Piramanayagam, Appl. Phys. Lett. **99**, 092506 (2011).

<sup>7</sup> S. Ikeda, K. Miura, H. Yamamoto, K. Mizunuma, H. D. Gan, M. Endo, S. Kanai, J. Hayakawa, F. Matsukura,

- and H. Ohno, *Nature Mater.* **9**, 721 (2010).
- <sup>8</sup> P. Nemeč, M. Fiebig, T. Kampfrath, and A. V. Kime, *Nat. Phys.* **14**, 229 (2018).
  - <sup>9</sup> C. Song, Y. F. You, X. Z. Chen, X. F. Zhou, Y. Y. Wang, and F. Pan, *Nanotechnology* **29**, 112001 (2018).
  - <sup>10</sup> S. A. Wolf, D. D. Awschalom, R. A. Buhrman, J. M. Daughton, S. von Molnar, M. L. Roukes, A. Y. Chtchelkanova, and D. M. Treger, *Science* **294**, 1488 (2001).
  - <sup>11</sup> V. Baltz, A. Manchon, M. Tsoi, T. Moriyama, T. Ono, and Y. Tserkovnyak, *Rev. Mod. Phys.* **90**, 015005 (2018).
  - <sup>12</sup> D. Hou, Z. Qiu, and E. Saitoh, *NPG Asia Mater.* **11**, 35 (2019).
  - <sup>13</sup> Y. Y. Wang, C. Song, B. Cui, G. Y. Wang, F. Zeng, and F. Pan, *Phys. Rev. Lett.* **109**, 137201 (2012).
  - <sup>14</sup> B. G. Park, J. Wunderlich, X. Marti, V. Holý, Y. Kurosaki, M. Yamada, H. Yamamoto, A. Nishide, J. Hayakawa, H. Takahashi, A. B. Shick, and T. Jungwirth, *Nat. Mater.* **10**, 347 (2011).
  - <sup>15</sup> J. Nogueš and I. K. Shuller, *J. Magn. Magn. Mater.* **192**, 203 (1999).
  - <sup>16</sup> A. Koziol-Rachwał, M. Szpytma, N. Spiridis, K. Freindl, J. Korecki, W. Janus, H. Nayyef, P. Drozd, M. Slezak, M. Zajac, and T. Slezak, *Appl. Phys. Lett.* **120**, 072404 (2022).
  - <sup>17</sup> L. Baldrati, A. Ross, T. Niizeki, C. Schneider, R. Ramos, J. Cramer, O. Gomonay, M. Filianina, T. Savchenko, D. Heinze, A. Kleibert, E. Saitoh, J. Sinova, and M. Klaui, *Phys. Rev. B* **98**, 014409 (2018).
  - <sup>18</sup> S. Mu, A. L. Wysocki, and K. D. Belashchenko, *Phys. Rev. B* **87**, 054435 (2013).
  - <sup>19</sup> M. Street, W. Echtenkamp, T. Komesu, S. Cao, P. A. Dowben, and Ch. Binek, *Appl. Phys. Lett.* **104**, 222402 (2014).
  - <sup>20</sup> S.-Q. Shi, A. L. Wysocki, and K. D. Belashchenko, *Phys. Rev. B* **79**, 104404 (2009).
  - <sup>21</sup> X. He, Y. Wang, N. Wu, A. N. Caruso, E. Vescovo, K. D. Belashchenko, P. A. Dowben, and Ch. Binek, *Nat. Mater.* **9**, 579 (2010).
  - <sup>22</sup> K. H. Wu, H.-J. Chen, Y. T. Chen, C. C. Hsieh, C. W. Luo, T. M. Uen, J. Y. Juang, J.-Y. Lin, T. Kobayashi, and M. Gospodinov, *Europhys. Lett.* **94**, 27006 (2011).
  - <sup>23</sup> S. J. May, P. J. Ryan, J. L. Robertson, J.-W. Kim, T. S. Santos, E. Karapetrova, J. L. Zarestky, X. Zhai, S. G. E. te Velthuis, J. N. Eckstein et al., *Nat. Mater.* **8**, 892 (2009).
  - <sup>24</sup> F. Maccherozzi, M. Sperl, G. Panaccione, J. Minar, S. Polesya, H. Ebert, U. Wurstbauer, M. Hochstrasser, G. Rossi, G. Woltersdorf, W. Wegscheider, and C. H. Back, *Phys. Rev. Lett.* **101**, 267201 (2008).
  - <sup>25</sup> K. Olejnik, P. Wadley, J. A. Haigh, K. W. Edmonds, R. P. Campion, A. W. Rushforth, B. L. Gallagher, C. T. Foxon, T. Jungwirth, J. Wunderlich, S. S. Dhesi, S. A. Cavill, G. van der Laan, and E. Arenholz, *Phys. Rev. B* **81**, 104402 (2010).
  - <sup>26</sup> P. K. Manna and S. M. Yusuf, *Physics Reports* **535**, 61 (2014).
  - <sup>27</sup> K. F. Eid, M. B. Stone, O. Maksimov, T. C. Shih, K. C. Ku, W. Fadgen, C. J. Palmstrom, P. Schiffer, and N. Samarth, *J. Appl. Phys.* **97**, 10D304 (2005).
  - <sup>28</sup> Hyuk J. Choi, R. K. Kawakami, Ernesto J. Escorcia-Aparicio, and Z. Q. Qiu, *Phys. Rev. Lett.* **82**, 1947 (1999).
  - <sup>29</sup> J. M. Vargas, J. Gomez, R. D. Zysler, and A. Butera, *Nanotechnology* **18**, 115714 (2007).
  - <sup>30</sup> J. Wu, G. S. Dong, and Xiaofeng Jin, *Phys. Rev. B* **70**, 212406 (2004).
  - <sup>31</sup> A. T. Hindmarch, K. J. Dempsey, J. P. Morgan, B. J. Hickey, D. A. Arena, and C. H. Marrows, *Appl. Phys. Lett.* **93**, 172511 (2008).
  - <sup>32</sup> B. B. Jena, S. Mandal, and K. S. R. Menon, *J. Phys. D: Appl. Phys.* **54**, 185001 (2021).
  - <sup>33</sup> B. B. Jena, A. Kar, S. Barman, S. Mandal, and K. S. R. Menon, *J. Phys. D: Appl. Phys.* **54**, 325001 (2021).
  - <sup>34</sup> Q. Li, J. H. Liang, Y. M. Luo, Z. Ding, T. Gu, Z. Hu, C. Y. Hua, H. -J. Lin, T. W. Pi, S. P. Kang, C. Won, and Y. Z. Wu, *Scientific Reports* **6**, 22355 (2016).
  - <sup>35</sup> J. Zhu, Q. Li, J. X. Li, Z. Ding, J. H. Liang, X. Xiao, Y. M. Luo, C. Y. Hua, H. -J. Lin, T. W. Pi, Z. Hu, C. Won, and Y. Z. Wu, *Phys. Rev. B* **90**, 054403 (2014).
  - <sup>36</sup> J. van Lierop, K. -W. Lin, J. -Y. Guo, H. Ouyang, and B. W. Southern, *Phys. Rev. B* **75**, 134409 (2007).
  - <sup>37</sup> K. Lenz, S. Zander, and W. Kuch, *Phys. Rev. Lett.* **98**, 237201 (2007).
  - <sup>38</sup> T. Nagamiya, K. Yosida, and R. Kubo, *Adv. Phys.* **4**, 1 (1955).
  - <sup>39</sup> A. J. Sievers and M. Tinkham, *Phys. Rev.* **129**, 1566 (1963).
  - <sup>40</sup> J. A. Borchers, M. J. Carey, R. W. Erwin, C. F. Majkrzak, and A. E. Berkowitz, *Phys. Rev. Lett.* **70**, 1878 (1993).
  - <sup>41</sup> M. Takano, T. Terashima, and Y. Bando, *Appl. Phys. Lett.* **51**, 205 (1987).
  - <sup>42</sup> C. A. Ramos, D. Lederman D, A. R. King, and V. Jaccarino, *Phys. Rev. Lett.* **65**, 2913 (1990).
  - <sup>43</sup> A. S. Carrigo and R. E. Camley, *Phys. Rev. B* **45**, 13117 (1992).
  - <sup>44</sup> E. N. Abarra, K. Takano, F. Hellman, and A. E. Berkowitz, *J. Appl. Phys.* **79**, 5919 (1996).
  - <sup>45</sup> E. N. Abarra, K. Takano, F. Hellman, and A. E. Berkowitz, *Phys. Rev. Lett.* **77**, 3451 (1996).
  - <sup>46</sup> M.J. Carey, A. E. Berkowitz, J. A. Borchers, and R. W. Erwin, *Phys. Rev. B* **47**, 9952 (1993).
  - <sup>47</sup> M. J. Carey and A. E. Berkowitz, *J. Appl. Phys.* **73**, 6892 (1993).
  - <sup>48</sup> J. Fujikata, K. Ishihara, K. Hayashi, H. Yamamoto, K. Yamada, *IEEE Trans. Magn.* **31**, 396 (1995).
  - <sup>49</sup> W. L. Roth, *J. Phys. Chem. Solids* **25**, 1 (1974).
  - <sup>50</sup> R. C. O'Handley, *Modern Magnetic Materials, Principles and Applications* (Wiley, New York, 2000).
  - <sup>51</sup> P. J. van der Zaag, Y. Ijiri, J. A. Borchers, L. F. Feiner, R. M. Wolf, J. M. Gaines, R. W. Erwin, M. A. Verheijen, *Phys. Rev. Lett.*, **84**, 6102 (2000).
  - <sup>52</sup> J. A. Borchers, R. W. Erwin, S. D. Berry, D. M. Lind, J. F. Ankner, E. Lochner, K. A. Shaw, D. Hilton, *Phys. Rev. B* **51**, 8276 (1995).
  - <sup>53</sup> I. P. Krug, F. U. Hillebrecht, H. Gomonaj, M. W. Haverkort, A. Tanaka, L. H. Tjeng, C. M. Schneider, *Euro. Phys. Lett.* **81**, 17005 (2008).
  - <sup>54</sup> A. R. Ball, A. J. G. Leenaers, P. J. van der Zaag, K. A. Shaw, B. Singer, D. M. Lind, H. Fredrikze, M. T. Rekveldt, *Appl. Phys. Lett.* **69**, 583 (1996).
  - <sup>55</sup> C. Gatel, E. Snoeck, V. Serin, A. R. Fert, *Eur. Phys. J B* **45**, 157 (2005).
  - <sup>56</sup> I. V. Golosovsky, G. Salazar-Alvarez, A. Lopez-Ortega, M. A. Gonzalez, J. Sort, M. Estrader, S. Surinach, M. D. Baro, and J. Nogueš, *Phys. Rev. Lett.* **102**, 247201 (2009).
  - <sup>57</sup> A. E. Berkowitz, G. F. Rodriguez, J. I. Hong, K. An, T. Hyeon, N. Agarwal, D. J. Smith, and E. E. Fullerton, *J. Phys. D: Appl. Phys.* **41**, 134007 (2008).
  - <sup>58</sup> K. Koike and T. Furukawa, *Phys. Rev. Lett.* **77**, 3921 (1996).
  - <sup>59</sup> A. Koziol-Rachwał, T. Slezak, T. Nozaki, S. Yuasa, and J.

- Korecki, *Appl. Phys. Lett.* **108**, 041606 (2016).
- <sup>60</sup> A. P. Malozemoff, *Phys. Rev. B* **37**, 7673 (1988).
- <sup>61</sup> U. Nowak, A. Misra, and K. D. Usadel, *J. Appl. Phys.* **89**, 7269 (2001).
- <sup>62</sup> C. Binek, A. Hochstrat, and W. Kleemann, *J. Magn. Magn. Mater* **234**, 353 (2001).
- <sup>63</sup> A. Mukherjee, N. D. Patel, S. Dong, S. Johnston, A. Moreo, and E. Dagotto, *Phys. Rev. B* **90**, 205133 (2014).
- <sup>64</sup> S. Chakraborty, A. Mukherjee, and K. Pradhan, *Phys. Rev. B* **106**, 075146 (2022).
- <sup>65</sup> S. Halder, S. Chakraborty, and K. Pradhan, *Phys. Rev. B* **110**, 195147 (2024).
- <sup>66</sup> S. Kumar and P. Majumdar, *Eur. Phys. J. B* **50**, 571 (2006).
- <sup>67</sup> K. Pradhan and A. P. Kampf, *Phys. Rev. B* **87**, 155152 (2013).
- <sup>68</sup> K. Pradhan and A. P. Kampf, *Phys. Rev. B* **88**, 115136 (2013).
- <sup>69</sup> S. Chakraborty, S. Halder, and K. Pradhan, *Phys. Rev. B* **108**, 165110 (2023).
- <sup>70</sup> S. Halder, Subrat K. Das, and K. Pradhan, *Phys. Rev. B* **108**, 235111 (2023).
- <sup>71</sup> G. D. Mahan, *Quantum Many Particle Physics* (Plenum Press, New York, 1990).
- <sup>72</sup> S. Kumar and P. Majumdar, *Europhys. Lett.* **65**, 75 (2004).
- <sup>73</sup> P. Bulanchuk, *Comput. Phys. Commun.* **261**, 107714 (2021).
- <sup>74</sup> S. R. White, D. J. Scalapino, R. L. Sugar, E. Y. Loh, J. E. Gubernatis, and R. T. Scalettar, *Phys. Rev. B* **40**, 506 (1989).
- <sup>75</sup> R. Mondaini and T. Paiva, *Phys. Rev. B* **95**, 075142 (2017).
- <sup>76</sup> G. Rohringer, A. Toschi, A. A. Katanin, and K. Held, *Phys. Rev. Lett.* **107**, 256402 (2011).
- <sup>77</sup> R. Staudt, M. Dzierzawa, and A. Muramatsu, *Eur. Phys. J. B* **17**, 411 (2000).
- <sup>78</sup> N. Yu, W. B. Zhang, N. Wang, Y. F. Wang, and B. Y. Tang, *J. Phys. Chem. C* **112**, 452 (2008).
- <sup>79</sup> A. Hermawan, A. T. Hanindriyo, E. R. Ramadhan, Y. Asakura, T. Hasegawa, K. Hongo, M. Inada, R. Maezonoc, and S. Yin, *Inorg. Chem. Front.* **7**, 3431 (2020).
- <sup>80</sup> S. L. Dudarev, G. A. Botton, S. Y. Savrasov, C. J. Humphreys, and A. P. Sutton, *Phys. Rev. B* **57**, 1505 (1998).
- <sup>81</sup> A. Rohrbach, J. Hafner, and G. Kresse, *Phys. Rev. B* **69**, 075413 (2004).
- <sup>82</sup> W. B. Zhang, Y. L. Hu, K. L. Han, and B. Y. Tang, *Phys. Rev. B* **74**, 139905 (2006).
- <sup>83</sup> K. L. Kostov, S. Polzin, S. K. Saha, O. Brovko, V. Stepanyuk, and W. Widdra, *Phys. Rev. B* **87**, 235416 (2013).
- <sup>84</sup> S. K. Saha, Valeri S. Stepanyuk, and J. Kirschner, *Physics Letters A* **378**, 3642 (2014).